SOFT ROBOTS

Inflatable soft jumper inspired by shell snapping

Benjamin Gorissen[1]*, David Melancon[1]*, Nikolaos Vasios[1], Mehdi Torbati[1], Katia Bertoldi[1,2,3]†

Fluidic soft actuators are enlarging the robotics toolbox by providing flexible elements that can display highly complex deformations. Although these actuators are adaptable and inherently safe, their actuation speed is typically slow because the influx of fluid is limited by viscous forces. To overcome this limitation and realize soft actuators capable of rapid movements, we focused on spherical caps that exhibit isochoric snapping when pressurized under volume-controlled conditions. First, we noted that this snap-through instability leads to both a sudden release of energy and a fast cap displacement. Inspired by these findings, we investigated the response of actuators that comprise such spherical caps as building blocks and observed the same isochoric snapping mechanism upon inflation. Last, we demonstrated that this instability can be exploited to make these actuators jump even when inflated at a slow rate. Our study provides the foundation for the design of an emerging class of fluidic soft devices that can convert a slow input signal into a fast output deformation.

INTRODUCTION

Inflatable soft actuators have emerged as an ideal platform to realize active structures capable of safe interactions with unstructured environments (*1*–*3*). Their compliance and ability to achieve complex deformations has enabled the design of flexible machines for a wide spectrum of applications (*4*), ranging from minimally invasive surgical tools (*5*) and exoskeletons (*6*) to warehouse grippers (*7*) and add-ons for video games (*8*). However, existing fluidic soft actuators are typically slow, because a substantial amount of fluid has to be supplied for their operation, the influx of which is restricted by viscous forces in tubes and valves. To overcome this limitation, it has been shown that fast actuation can be achieved either by modifying the geometry to reduce the amount of fluid needed for inflation (*9*) or by using chemical reactions to generate explosive bursts of pressure (*10*). Alternatively, snapping instabilities can also provide a powerful nonlinear mechanism that decouples the slow input signal from the output deformation and triggers rapid events (*11*–*15*).

Inspired by recent progress using snapping instabilities to increase the speed of actuation (*11*, *16*), we investigated the snapping of spherical caps as a mechanism to realize fluidic soft actuators capable of rapid movements. We first showed that the snapping of elastomeric spherical caps upon pressurization results in a sudden release of energy, the amount of which can be controlled by tuning the caps' geometry, material stiffness, and boundary conditions at the edges. We then realized fluidic soft actuators by combining two spherical caps (see Fig. 1A) and found that the energy released upon snapping of the inner cap leads to a rapid inversion of its pole that ultimately enables jumping. Last, we identified geometric and material parameters that result in substantial energy release and jump height, providing a rich design domain for fluidic soft actuators capable of extremely fast movements regardless of inflation rate.

[1]J.A. Paulson School of Engineering and Applied Sciences, Harvard University, Cambridge, MA 02138, USA. [2]Wyss Institute for Biologically Inspired Engineering, Harvard University, Cambridge, MA 02138, USA. [3]Kavli Institute for Bionano Science and Technology, Harvard University, Cambridge, MA 02138, USA.
*These authors contributed equally to this work.
†Corresponding author. Email: bertoldi@seas.harvard.edu

RESULTS

Snapping of spherical caps as a platform for fast fluidic soft robots

To create fast inflatable soft actuators, we started by conducting finite element (FE) analyses to investigate the response upon pressurization of elastomeric spherical caps with radius, R, thickness, t, and polar angle, θ (see Fig. 1B). In our simulations (which were conducted using the commercial package ABAQUS 2018/Standard), we assumed the deformation to be axisymmetric, discretized the models with four-node bilinear axisymmetric solid elements, and used an incompressible Gent material model with initial shear modulus, μ (*17*). We pressurized the caps by supplying incompressible fluid to a cavity above them (highlighted in gray in the inset in Fig. 1B) and simulated the quasi-static pressure-volume curve via the modified Riks algorithm (*18*, *19*). In Fig. 1B, we consider a thin cap with polar angle $\theta = 60^\circ$, normalized radius $\eta = R/t = 30$, and clamped boundary conditions at the base. We found that the pressure-volume curve of this cap is qualitatively identical to those recently reported for pressurized spherical shells (*20*–*22*) and is characterized by a limit point when inflating under volume-controlled conditions (indicated by a black circular marker in Fig. 1B). This volume limit causes an instability, leading the system to snap to a point of lower pressure (white circular marker in Fig. 1B). This occurs while conserving the volume in the cavity and results in a partial inversion of the cap, which we characterize by quantifying the distance traveled by the pole during the instability, Δy_{pole} (see insets in Fig. 1B). Further, we note that the isochoric snapping of the cap is accompanied by a sudden release of energy, ΔE, that graphically corresponds to the green highlighted area in Fig. 1B and can be obtained as

$$\Delta E = \int_{\Gamma} p \, d\Delta V \tag{1}$$

where Γ is the equilibrium path that connects the limit point in volume and the corresponding isochoric point on the lower branch (highlighted by a dashed black line in Fig. 1B). For the considered cap, we find $\Delta E = 1.50 \times 10^{-5} \mu R^3$ and $\Delta y_{pole} = 1.31 \times 10^{-1} R$.

Next, to investigate the effect of geometry on ΔE and Δy_{pole}, we compared the response of the thin spherical cap with that of a thicker one with $\eta = 8.5$ and both with clamped and roller boundary conditions at the base. The results reported in Fig. 1C indicate that the

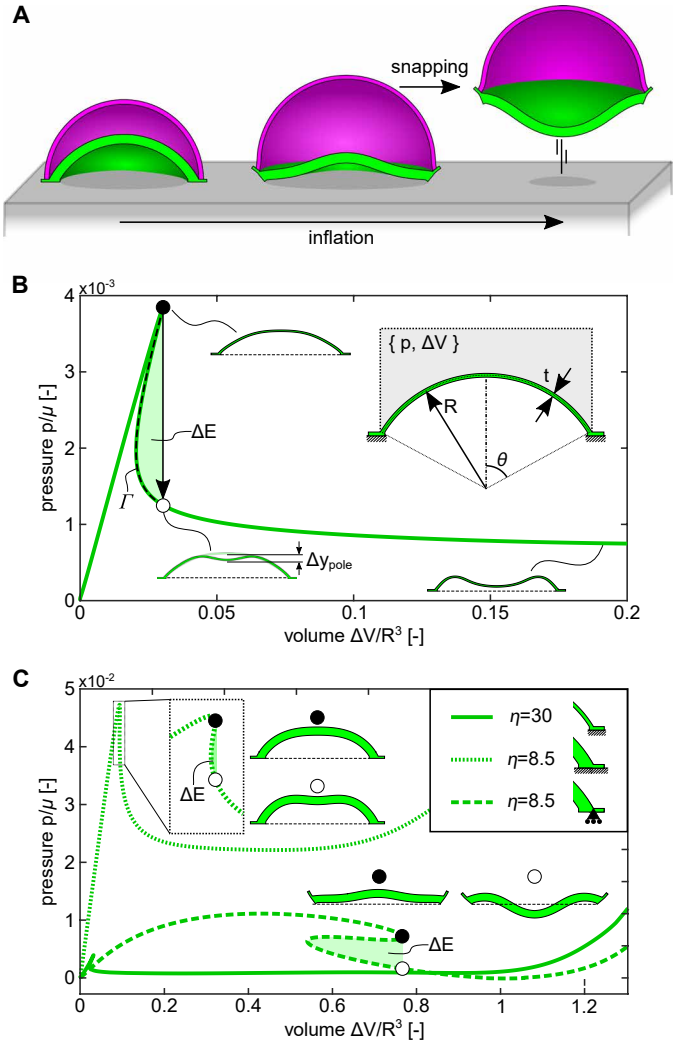

Fig. 1. Snapping of spherical caps for fast fluidic soft robots. (**A**) Our soft fluidic actuators comprise two spherical caps connected at their base. Upon inflation, the inner cap snaps and enables our simple device to take off. (**B**) The pressure-volume curve, normalized by initial shear modulus, μ, and radius, *R*, of a given pressurized spherical cap is characterized by a limit point when inflating under volume-controlled conditions. This volume limit point causes an isochoric snapping instability, which leads to a sudden release of energy, Δ*E* (highlighted in green), and the inversion of the inner cap (which we characterize by quantifying the distance travelled by the cap's pole, Δy_{pole}). (**C**) Comparison between the pressure-volume curves of thin (solid green line) and thick spherical caps with both clamped (dotted green line) and roller (dashed green line) boundary conditions. Note that the normalized radius η is defined as the ratio of cap radius over cap thickness (i.e., $\eta = R/t$).

boundary conditions play a major role on the snapping behavior. The clamped thick cap is characterized by a very large maximum pressure, but a very small energy release and pole displacement upon snapping ($\Delta E = 4.78 \times 10^{-6} \mu R^3$ and $\Delta y_{pole} = 6.30 \times 10^{-2} R$). On the other hand, roller boundary conditions lower the maximum pressure but lead to a much higher energy release and pole displacement ($\Delta E = 8.00 \times 10^{-4} \mu R^3$ and $\Delta y_{pole} = 2.67 \times 10^{-1} R$). As a result, our simulations indicate not only that isochoric snapping of spherical caps provides opportunities to realize systems capable of suddenly releasing a substantial amount of energy through their inversion but also that by tuning geometry and boundary conditions, we can control and maximize the response of these systems.

Inflatable soft actuators inspired by shell snapping

Having demonstrated numerically that snapping of a spherical cap results in a sudden energy release and pole displacement, we then investigated the mechanical response of fully soft actuators comprising two spherical caps connected at their base to form a cavity that we inflate with an incompressible fluid (see Fig. 1A). We began by considering three actuators with inner caps identical to those introduced in Fig. 1C (with $R_i = 30$ mm) with outer caps characterized by $\theta_o = 90^\circ$ and $\eta_o = 16.5$ (note that here and in the following, the subscripts o and i are used to indicate properties of the outer and inner caps, respectively). Specifically, design A has a thin inner cap with $\theta_i = 60^\circ$ and $\eta_i = 30$, whereas designs B and C have a thick cap with $\theta_i = 60^\circ$ and $\eta_i = 8.5$. Further, we assumed that both caps of designs A and B are made of the same elastomeric material (i.e., $\mu_i/\mu_o = 1$); however, for design C, we consider an outer cap made of a softer rubber, resulting in $\mu_i/\mu_o = 5.8$. The numerically obtained pressure-volume curves for the three actuators (shown in Fig. 2A as blue lines) share many features with those reported in Fig. 1C for the individual pressurized caps and are all characterized by a limit point near the maximum pressure when considering volume-controlled conditions. Hence, our actuators also exhibit isochoric snapping upon inflation, and this again results in a sudden release of elastic energy and the inversion of the inner cap. By comparing the responses of the three actuators, we find that design C exhibits the largest energy release and displacement of the inner cap's pole (Δ*E* = 0.875, 5.67, and 31.4 mJ for designs A, B, and C, respectively, whereas Δy_{pole} = 7.68, 7.55, and 20.89 mm for designs A, B, and C, respectively). These results agree with the trends observed for the individual pressurized caps (see Fig. 1C), because both Δ*E* and Δy_{pole} increase for thicker caps that are allowed to rotate at their base (note that in our actuators, such boundary conditions are not directly controlled but rather determined by the outer cap; see fig. S13). Furthermore, the results highlight the important role of the outer caps and indicate that both Δ*E* and Δy_{pole} can be enhanced by increasing their compliance. This is because compliant outer caps can sustain more deformation before snapping (see insets in Fig. 2A) and, therefore, enable the actuator to store more elastic energy that can be potentially released upon instability.

Next, to experimentally validate our analyses, we fabricated the three actuators using molds and inflated them with water while submerged in water to eliminate the effects of gravity (see the Supplementary Materials for details). In this experimental analysis, all caps were fabricated out of Zhermack Elite Double 32 (with green color and initial shear modulus μ = 0.35 MPa), except for the outer cap of design C, where we used Zhermack Elite Double 8 (with purple color and initial shear modulus μ = 0.06 MPa). Note that these values were obtained by minimizing the error between experiments and simulations for design C and are within the range previously reported in the literature (*21*, *23*–*25*). In Fig. 2A, we compare the numerical (blue lines) and experimental (red lines) pressure-volume curves for the three actuators, whereas in Fig. 2B, we display snapshots that are taken during the tests. We found good agreement between simulations and experiments, with pressure measurements that show a sudden drop near the numerically predicted limit point. The small discrepancies between experiments and simulations can be attributed to unavoidable imperfections introduced during fabrication,

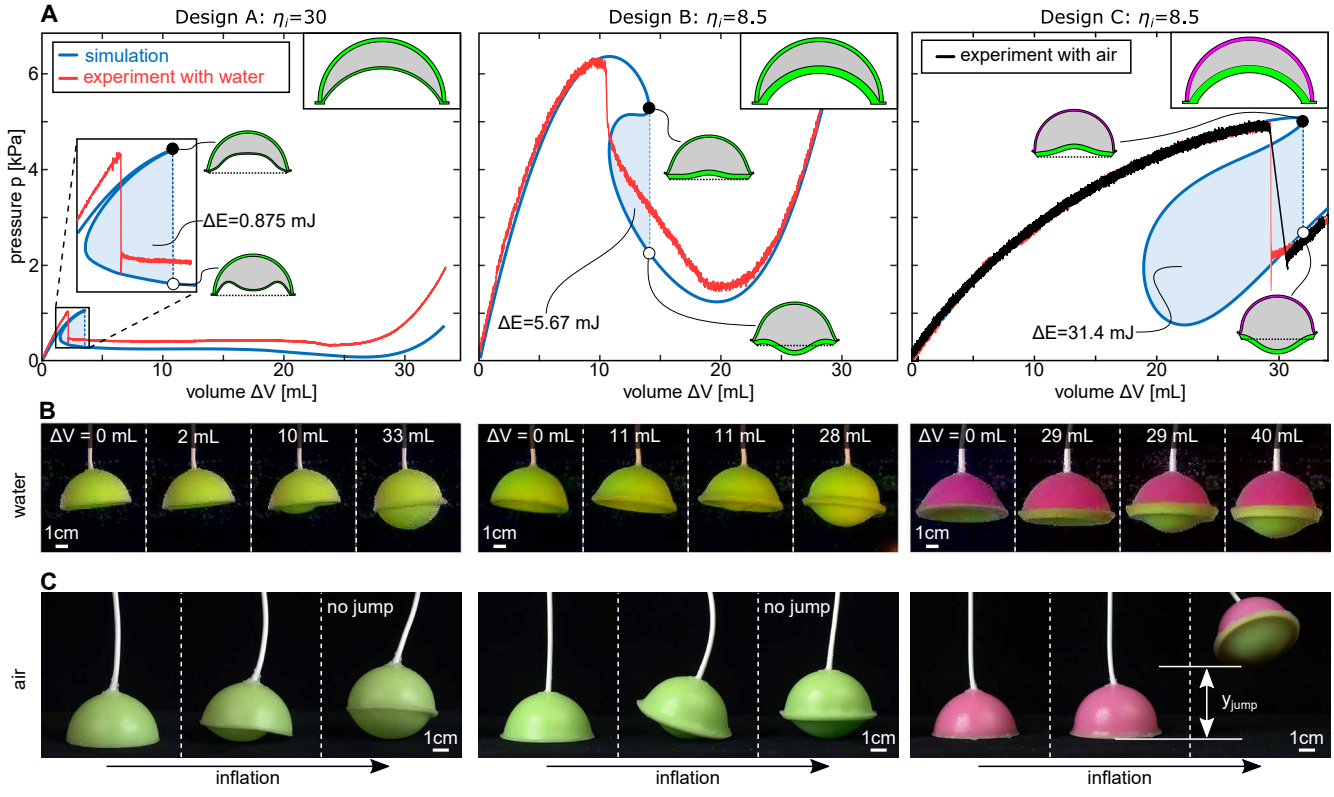

Fig. 2. Our inflatable soft actuators. (**A**) Experimental (red) and numerical (blue) pressure-volume curves for the inflation with water of three actuators (all with inner cap radius R_i = 30 mm) characterized by normalized radii, polar angles, and ratio of shear moduli (η_i, θ_i, η_o, θ_o, μ_i/μ_o) = (30, 60˚, 16.5, 90˚, 1) (design A), (8.5, 60˚, 16.5, 90˚, 1) (design B), and (8.5, 60˚, 16.5, 90˚, 5.8) (design C). The energy released upon snapping, ΔE, is highlighted by the shaded blue region. The volume limit point upon inflation is identified with a black circular marker, whereas its corresponding isochoric point on the lower branch is identified with a white circular marker. For design C, we also report the experimental pressure-volume curve obtained when inflating the actuator with air (black line). (**B**) Experimental snapshots of the three design during inflation with water at different amounts of supplied fluid. (**C**) Experimental snapshots of the three designs during inflation with air. The isochoric snapping makes design C jump and reach a maximum height denoted y_{jump}.

visco-elasticity of the rubber, and slight asymmetric buckling of the inner cap. Furthermore, in all of our tests, as observed in the simulations, snapping is also accompanied by the sudden inversion of the inner cap. For design A, Δy_{pole} is such that the inner cap's pole remains above the base plane of the actuator upon snapping; for designs B and C, however, the large value of Δy_{pole} allows for their inner cap's pole to cross it (see Fig. 2B).

Motivated by these results, we investigated how snapping can be exploited to enhance the functionality of our simple robots and to make them jump even when inflated at a slow rate. To this end, we positioned our actuators on a flat surface and slowly inflated them with air (see the Supplementary Materials for details). The snapshots reported in Fig. 2C reveal that, despite the slow rate of inflation (10 ml/min with a syringe pump), the isochoric snapping makes design C jump and reach a maximum height of y_{jump} = 42.9 mm. On the other hand, although the inner cap of designs A and B snaps upon inflation, their ΔE and Δy_{pole} are not large enough to enable them to take off. Although this last set of tests was conducted using a compressible fluid (air), the effect of fluid compressibility on the response of the system's energy release was negligible and only led to a slight increase of volume during snap-through (see Fig. 2A and the Supplementary Materials for details). Hence, the experiments and analyses conducted using an incompressible fluid can be also used to understand and improve the performance of our air-inflated jumpers.

Improving the actuators' response

Thus far, we have shown that the geometry and material properties of the caps strongly affect the snapping behavior and that by tuning ΔE and Δy_{pole}, we can harness the instability to make our actuators jump. Motivated by these findings, we proceeded by systematically exploring the parameter space to identify designs that can jump higher than design C. Figure 2C indicates that jumping requires large enough ΔE and Δy_{pole}, and Fig. 2A indicates that ΔE and Δy_{pole} can be enhanced by combining an inner cap that releases a large amount of energy upon snapping with an outer cap that stores a large amount of energy before snapping. Therefore, we started by considering the two caps separately and used axisymmetric FE analyses to investigate their behavior for a wide range of geometric parameters (i.e., $40^\circ \le \theta_i \le 80^\circ$, $5 \le \eta_i \le 12.5$, $40^\circ \le \theta_o \le 90^\circ$, and $5 \le \eta_o \le 20$).

Focusing on the inner cap, we found that by varying θ_i and η_i, its response undergoes several transitions (see Fig. 3, A and B). For low values of θ_i and η_i (i.e., for thick and shallow caps), the inner cap does not exhibit isochoric snapping (see light gray region in Fig. 3, A and B). By increasing θ_i at constant η_i, snapping is eventually triggered upon inflation. Within this domain, both the energy released by the inner cap, ΔE_i, and its pole displacement, Δy_{pole}, increase monotonically as a function of θ_i, suggesting that the response of our actuators can be enhanced by considering deep and sufficiently thick inner caps. Last, for high values of θ_i and η_i (i.e., for thin and deep caps), the

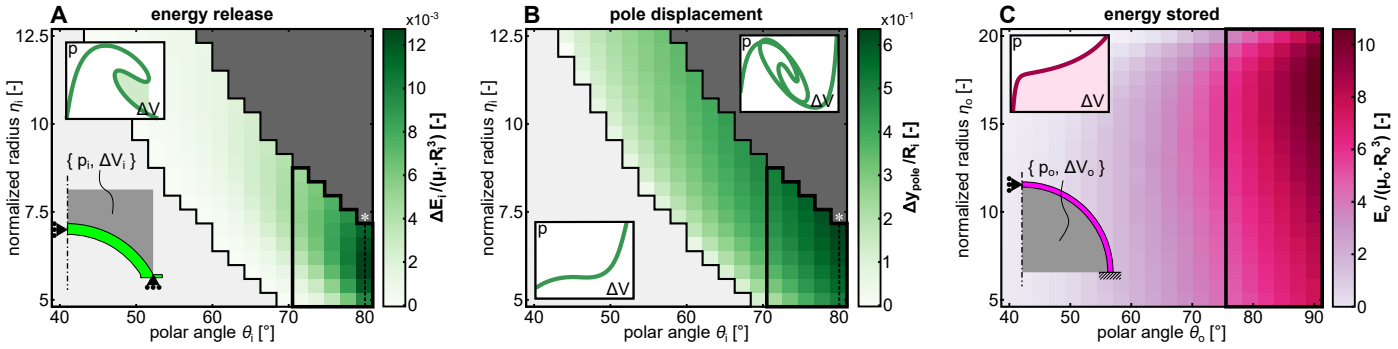

Fig. 3. Mechanical response of the inner and outer caps upon inflation. (**A** and **B**) Evolution of the inner cap's normalized (A) energy release, $\Delta E_i/(\mu_i R_i^3)$, and (B) pole displacement, $\Delta y_{pole}/R_i$, upon snapping as a function of the normalized radius, η_i, and the polar angle, θ_i. (**C**) Evolution of the outer cap's normalized stored energy at $p/\mu_o = 0.5$, $E_o/(\mu_o R_o^3)$, as a function of the normalized radius, η_o, and the polar angle, θ_o.

pressure-volume curves become self-crossing (see dark gray region in Fig. 3, A and B), which is an indication of the existence of a more favorable asymmetric deformation path with low ΔE_i and Δy_{pole} (see fig. S16).

Next, we turned our attention to the outer cap and found that its response is less rich and resembles that of an inflated thin spherical balloon (*26*, *27*). Because the outer cap in our actuators acts as an energy reservoir, in Fig. 3C, we report the evolution of the stored energy in the outer cap, E_o, at a normalized pressure of $p/\mu_o = 0.5$, as a function of the polar angle, θ_o, and the normalized radius, η_o. The results indicate that E_o increases monotonically with θ_o (almost irrespective of η_o), therefore suggesting that the response of our actuators can be enhanced by focusing on deep outer caps.

Although the results of Fig. 3 enabled us to identify promising regions of the design space (i.e., inner caps with $\theta_i \geq 70^\circ$ and $\eta_i \leq 8$ and outer ones with $\theta_o \geq 76^\circ$), they could not be directly used to realize the best possible jumper because they neglect the coupling between the two caps. Therefore, as next step, we used axisymmetric FE analyses to simulate the response of 4800 actuators constructed by combining inner and outer caps within the identified promising regions (highlighted by black contours in Fig. 3). In Fig. 4A, we report ΔE and Δy_{pole} for all simulated actuators with both $\mu_i/\mu_o = 1$ (green markers) and 5.8 (purple markers). Four key features emerge from the plot. First, by comparing the results with those obtained for the three actuators considered in Fig. 2 (indicated by square markers in Fig. 4A), we find that both ΔE and Δy_{pole} can be greatly increased when the geometry is properly tuned. Second, the results show that, on one hand, there is a strong correlation between ΔE and Δy_{pole} and, on the other hand, there is a disconnection between them and the drop in pressure associated with the snapping instability. Specifically, by inspecting the pressure-volume curves for the actuators (shown as insets in Fig. 4A), we found that for the designs with large ΔE and Δy_{pole}, the drop in pressure is small, whereas the area enclosed by the pressure-volume curve between the limit point and the corresponding isochoric point on the lower branch is large. Third, the results confirmed the importance of a flexible outer cap because both ΔE and Δy_{pole} span a much larger domain for the actuators with $\mu_i/\mu_o = 5.8$. Fourth, we found that the inner cap plays a crucial role and that by choosing $\theta_i = 80^\circ$ to optimize its response, we can further improve the performance of the actuators (see black contour markers in Fig. 4A). At the same time, however, the results also highlight that for actuators with $\mu_i/\mu_o = 5.8$, the outer cap geometry is important, because some design choices lead to noticeably lower ΔE and Δy_{pole}.

Our quasi-static FE simulations allowed us to efficiently explore the design space and calculate ΔE and Δy_{pole} for a large number of designs. However, because they do not account for dynamic effects, they cannot be used to directly characterize the ability of the actuators to jump. To overcome this limitation, we established a simple mass-spring model that takes the FE results of Fig. 4A as input and predicts the jump height, y_{jump}. This reduced order model comprises two concentrated masses, m_i and m_o, connected by a spring with stiffness k_s and rest length L_0 (Fig. 4B). We chose m_i and m_o to be equal to the mass of the inner and outer cap, respectively, and to be located at their corresponding poles. We then focused on the numerically predicted configurations immediately before and after snapping and assumed that the mechanical system stores an amount of energy equal to ΔE in the former and is stress free in the latter. It follows that L_0 is equal to the distance between the poles immediately before snapping and that (see Fig. 4B)

$$k_s = \frac{2\Delta E}{(\Delta y_{pole})^2}. \quad (2)$$

Last, we consider the spring to be initially precompressed by Δy_{pole} and m_i to be positioned at a distance h_{imp} from the ground (h_{imp} being the numerically predicted distance of the inner cap's pole from the ground immediately before snapping). At time $t = 0$, we released the system and analytically determined the position of the two masses, $y_i(t)$ and $y_o(t)$, as a function of time while accounting for contact with a rigid surface.

To verify the validity of our simplified mass-spring model, we first focused on three designs with (η_i, θ_i, η_o, θ_o, μ_i/μ_o) = (8.5, 60°, 16.5, 90°, 5.8) (design C), (5.4, 80°, 15.3, 87°, 5.8), and (5.8, 80°, 10.5, 85°, 5.8) and compared the experimentally measured jump heights (h_{jump} = 42.9, 160, and 209 mm, respectively) to the predicted ones. When choosing a coefficient of restitution $\alpha = 0.5$ and approximating the effect of dissipation with a linear dashpot with damping coefficient $c_d = 0.4$ kg/s, we found excellent agreement between the two sets of data, with the model predicting $y_{jump} = \max(y_i(t)) = 41.4$, 175, and 226 mm (see the Supplementary Materials for details). Hence, these results indicate that our simple mass-spring model, despite the fact that it cannot capture the complex dynamic behavior typical of shells (*14*, *28*, *29*), can accurately predict the jump height

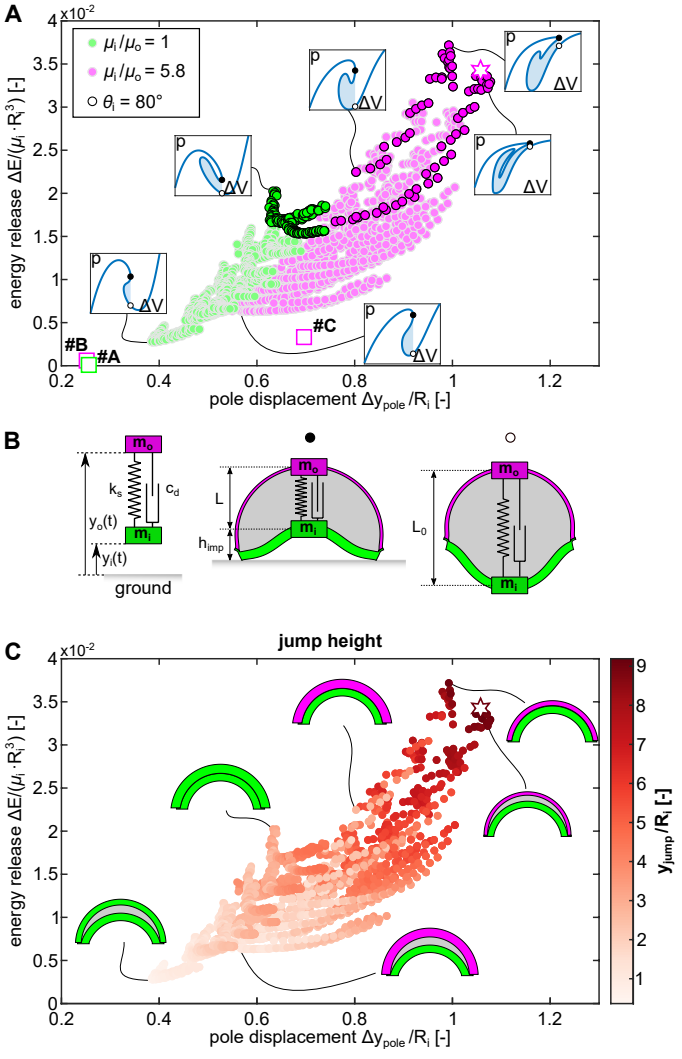

Fig. 4. Improving the response of the actuators. (**A**) Normalized energy release, $\Delta E/(\mu_i R_i^3)$, versus normalized pole displacement, $\Delta y_{pole}/R_i$, for actuators with inner polar angle $\theta_i \geq 70^\circ$, normalized inner radius $\eta_i \leq 8$, and normalized outer radius $\theta_o \geq 76^\circ$. (**B**) Reduced order mass-spring model used to predict jump height based on the numerical results reported in (A). The model comprises two masses m_i and m_o connected via a spring with stiffness k_s and a dashpot with damping coefficient c_d. (**C**) Normalized jump height, y_{jump}/R_i, as a function of energy release and pole displacement for the 4800 actuators considered in (A).

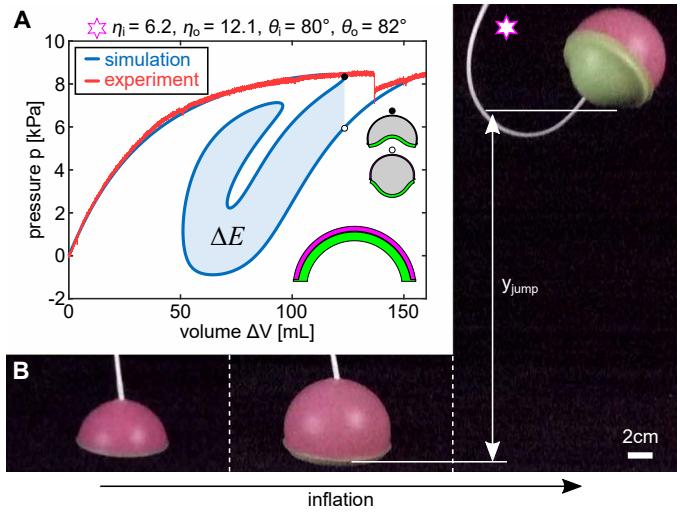

Fig. 5. Actuator with highest jump height. (**A**) Numerical (blue line) and experimental (red line) pressure-volume curves for the actuator with normalized radii, polar angles, and ratio of shear moduli (η_i, θ_i, η_o, θ_o, μ_i/μ_o) = (6.2, 80°, 12.1, 82°, 5.8) and inner cap radius R_i= 30 mm. (**B**) Experimental snapshots of the actuator upon inflation with air.

of our soft jumpers. Having confirmed the validity of our model, we then used it to calculate the y_{jump} for all 4800 actuators considered in Fig. 4A. The results reported in Fig. 4C indicate that a high jump requires both ΔE and Δy_{pole} to be large. Specifically, we found that the jump height is highest for an actuator with (η_i, θ_i, η_o, θ_o, μ_i/μ_o) = (6.2, 80°, 12.1, 82°, 5.8) for which ΔE = 324 mJ and Δy_{pole} = 31.7 mm. For such an actuator, our model predicts y_{jump} = 275 mm, a jump height that is one order of magnitude larger than that previously recorded for design C. Our experimental results fully confirmed the numerical predictions for this design for both the pressure-volume curve (see Fig. 5A) and the jump height y_{jump} = 283 mm (see Fig. 5B), further reinforcing the validity and efficiency of our numerical scheme to identify actuators with improved performance.

CONCLUSION

In summary, we have introduced a new family of inflatable soft actuators that harness isochoric snapping to move rapidly and even jump when inflated slowly. This behavior is encoded in their pressure-volume relationship, which exhibits two limit points in volume. Although fluidic actuators are typically characterized by a monotonic pressure-volume curve (*9*, *30*), it has been recently shown that limit points in pressure can be exploited to enhance their functionality and enable sequencing (*31*–*33*). Here, we show that by introducing limit points in volume, we can realize soft robots capable of suddenly releasing a given amount of energy. Because the instability occurs at constant volume and does not involve transfer of fluid, the release of energy is extremely fast and enables us to convert the slow input signal into exceptionally rapid events such as jumps. Last, our actuators can be simply reset and brought back to the initial configuration through vacuum and, therefore, can take off repetitively (see movie S6).

In this study, we have demonstrated the concept for spherical caps at the centimeter scale; however, our approach can be extended to any shape and does not depend on size. Because both ΔE and the gravitational potential energy are proportional to the mass, the jump height is independent of size (*34*). Thus, we expect the relative jump, y_{jump}/R_i, to monotonically increase as the actuators are scaled down. On the other hand, on-board actuation and control may be embedded in larger jumpers (as the mass of these additional elements become negligible compared with that of the actuators) and open the way to real-world applications requiring untethered soft robots (*35*, *36*). Last, in this work we have focused on the response of spherical caps under inflation; however, similar highly nonlinear behavior (i.e., force-displacement curves characterized by limit points in displacement) has been reported for the indentation of shallow arches (*37*) and shells with curved creases (*38*). Because structural elements with limit points in force have already been used to realize mechanical metamaterials with unique properties (*39*–*43*), we believe that by

integrating these new building blocks into their design, we can further expand their modes of functionality.

MATERIALS AND METHODS

Details of the design, materials, and fabrication methods are summarized in sections S1 and S2. The experimental procedures, including the inflation with water to measure the pressure-volume curve and the inflation with air to measure jump height, are described in section S3. FE procedures and jumper mass-spring model are detailed in sections S4 and S5. Validation of the FE model and jumper mass-spring model is reported in section S6.

SUPPLEMENTARY MATERIALS

robotics.sciencemag.org/cgi/content/full/5/42/eabb1967/DC1
Section S1. Design
Section S2. Fabrication
Section S3. Testing
Section S4. FE simulations
Section S5. Mass-spring model to predict the jump height
Section S6. Additional results
Fig. S1. Ideal design of the inflatable actuators.
Fig. S2. Manufacturable design of the inflatable actuators.
Fig. S3. Fabrication of the inflatable actuators.
Fig. S4. Baseline designs of the inflatable actuators.
Fig. S5. Experimental setup of the inflation with water.
Fig. S6. Experimental pressure-volume curves of the inflatable actuators.
Fig. S7. Experimental setup of the inflation with air.
Fig. S8. Jumping tests of the inflatable actuators.
Fig. S9. Effect of air compressibility.
Fig. S10. Numerical and experimental pressure-volume curves of the inflatable actuators.
Fig. S11. Pole displacement of the inflatable actuators.
Fig. S12. Three-dimensional simulations of the inflatable actuators.
Fig. S13. Axisymmetric simulations of the inflatable actuators.
Fig. S14. Extracting ΔE from the numerical *p-v* curves.
Fig. S15. Axisymmetric simulations of the inner cap.
Fig. S16. Asymmetric deformation emerges in designs with self-crossing pressure-volume curves.
Fig. S17. Axisymmetric simulations of the outer cap.
Fig. S18. Mass-spring model to predict jump height.
Fig. S19. Jump height prediction of the inflatable actuators.
Fig. S20. Validation of the spring-mass model.
Fig. S21. Improving the performance our soft fluidic actuators through a grid search.
Fig. S22. Influence of the outer cap stiffness on the actuators' response.
Movie S1. Snapping of spherical caps results in a sudden release of elastic energy.
Movie S2. Fast fluidic soft robots inspired by shell snapping.
Movie S3. Isochoric snapping enables jumping in fluidic soft robots.
Movie S4. Simplified mass-spring model to predict jump height.
Movie S5. Improving jumper design to increase jump height.
Movie S6. Inflatable actuator with repetitive jumping.

REFERENCES AND NOTES

1. D. Rus, M. T. Tolley, Design, fabrication and control of soft robots. *Nature* **521**, 467–475 (2015).
2. C. Majidi, Soft robotics: A perspective—current trends and prospects for the future. *Soft Robot.* **1**, 5–11 (2014).
3. D. Trivedi, C. D. Rahn, W. M. Kier, I. D. Walker, Soft robotics: Biological inspiration, state of the art, and future research. *Appl. Bionics Biomech.* **5**, 99 (2008).
4. B. Gorissen, D. Reynaerts, S. Konishi, K. Yoshida, J. W. Kim, M. De Volder, Elastic inflatable actuators for soft robotic applications. *Adv. Mater.* **29**, 1604977 (2017).
5. M. Runciman, A. Darzi, G. P. Mylonas, Soft robotics in minimally invasive surgery. *Soft Robot.* **6**, 423–443 (2019).
6. P. Polygerinos, Z. Wang, K. C. Galloway, R. J. Wood, C. J. Walsh, Soft robotic glove for combined assistance and at-home rehabilitation. *Robot. Auton. Syst.* **73**, 135–143 (2015).
7. E. Brown, N. Rodenberg, J. Amend, A. Mozeika, E. Steltz, M. R. Zakin, H. Lipson, H. M. Jaeger, Universal robotic gripper based on the jamming of granular material. *Proc. Natl. Acad. Sci. U.S.A.* **107**, 18809–18814 (2010).
8. J. Barreiros, H. Claure, B. Peele, O. Shapira, J. Spjut, D. Luebke, M. Jung, R. Shepherd, Fluidic elastomer actuators for haptic interactions in virtual reality. *IEEE Robot. Autom. Lett.* **4**, 277–284 (2019).
9. B. Mosadegh, P. Polygerinos, C. Keplinger, S. Wennstedt, R. F. Shepherd, U. Gupta, J. Shim, K. Bertoldi, C. J. Walsh, G. M. Whitesides, Pneumatic networks for soft robotics that actuate rapidly. *Adv. Funct. Mater.* **24**, 2163–2170 (2014).
10. R. F. Shepherd, A. A. Stokes, J. Freake, J. Barber, P. W. Snyder, A. D. Mazzeo, L. Cademartiri, S. A. Morin, G. M. Whitesides, Using explosions to power a soft robot. *Angew. Chem. Int. Ed.* **52**, 2892–2892 (2013).
11. J. T. Overvelde, T. Kloek, J. J. D'haen, K. Bertoldi, Amplifying the response of soft actuators by harnessing snap-through instabilities. *Proc. Natl. Acad. Sci. U.S.A.* **112**, 10863–10868 (2015).
12. P. Rothemund, A. Ainla, L. Belding, D. J. Preston, S. Kurihara, Z. Suo, G. M. Whitesides, A soft, bistable valve for autonomous control of soft actuators. *Sci. Robot.* **3**, eaar7986 (2018).
13. Y. Forterre, J. M. Skotheim, J. Dumais, L. Mahadevan, How the venus flytrap snaps. *Nature* **433**, 421–425 (2005).
14. A. Pandey, D. E. Moulton, D. Vella, D. P. Holmes, Dynamics of snapping beams and jumping poppers. *EPL* **105**, 24001 (2014).
15. D. Vella, Buffering by buckling as a route for elastic deformation. *Nat. Rev. Phys.* **1**, 425–436 (2019).
16. H. Lee, C. Xia, N. X. Fang, First jump of microgel; actuation speed enhancement by elastic instability. *Soft Matter* **6**, 4342–4345 (2010).
17. A. N. Gent, A new constitutive relation for rubber. *Rubber Chem. Technol.* **69**, 59–61 (1996).
18. E. Riks, An incremental approach to the solution of buckling and snapping problems. *Int. J. Solids Struct.* **15**, 524–551 (1979).
19. M. A. Crisfield, A fast incremental/iterative solution procedure that handles snap-through. *Comput. Struct.* **13**, 55–62 (1983).
20. J. W. Hutchinson, Buckling of spherical shells revisited. *Proc. R. Soc. A* **472**, 20160577 (2016).
21. A. Lee, F. L. Jiménez, J. Marthelot, J. W. Hutchinson, P. M. Reis, The geometric role of precisely engineered imperfections on the critical buckling load of spherical elastic shells. *J. Appl. Mech.* **83**, 111005 (2016).
22. R. Zoelly, Ueber ein knickungsproblem an der kugelschale, thesis, ETH Zurich (1915).
23. B. Florijn, C. Coulais, M. van Hecke, Programmable mechanical metamaterials. *Phys. Rev. Lett.* **113**, 175503 (2014).
24. L. Stein-Montalvo, P. Costa, M. Pezzulla, D. P. Holmes, Buckling of geometrically confined shells. *Soft Matter* **15**, 1215–1222 (2019).
25. J. T. B. Overvelde, D. M. J. Dykstra, R. de Rooij, J. Weaver, K. Bertoldi, Tensile instability in a thick elastic body. *Phys. Rev. Lett.* **117**, 094301 (2016).
26. A. Needleman, Inflation of spherical rubber balloons. *Int. J. Solids Struct.* **13**, 409–421 (1977).
27. I. Müller, P. Strehlow, *Rubber and Rubber Balloons: Paradigms of Thermodynamics* (Springer Science & Business Media, 2004), vol. 637.
28. M. Gomez, D. E. Moulton, D. Vella, Dynamics of viscoelastic snap-through. *J. Mech. Phys. Solids* **124**, 781–813 (2019).
29. D. Karagiozova, X.-W. Zhang, T.-X. Yu, Static and dynamic snap-through behaviour of an elastic spherical shell. *Acta Mech. Sinica* **28**, 695–710 (2012).
30. N. Vasios, A. J. Gross, S. Soifer, J. T. Overvelde, K. Bertoldi, Harnessing viscous flow to simplify the actuation of fluidic soft robots. *Soft Robot.* **7**, 1–9 (2019).
31. B. Gorissen, E. Milana, A. Baeyens, E. Broeders, J. Christiaens, K. Collin, D. Reynaerts, M. De Volder, Hardware sequencing of inflatable nonlinear actuators for autonomous soft robots. *Adv. Mater.* **31**, 1804598 (2019).
32. L. Hines, K. Petersen, M. Sitti, Inflated soft actuators with reversible stable deformations. *Adv. Mater.* **28**, 3690–3696 (2016).
33. E. Ben-Haim, L. Salem, Y. Or, A. D. Gat, Single-input control of multiple fluid-driven elastic actuators via interaction between bistability and viscosity. *Soft Robot.* **7**, 259–265 (2019).
34. S. Mahajan, *The Art of Insight in Science and Engineering: Mastering Complexity* (MIT Press, 2014).
35. A. Rafsanjani, Y. Zhang, B. Liu, S. M. Rubinstein, K. Bertoldi, Kirigami skins make a simple soft actuator crawl. *Sci. Robot.* **3**, eaar7555 (2018).
36. M. T. Tolley, R. F. Shepherd, B. Mosadegh, K. C. Galloway, M. Wehner, M. Karpelson, R. J. Wood, G. M. Whitesides, A resilient, untethered soft robot. *Soft Robot.* **1**, 213–223 (2014).
37. R. M. Neville, R. M. Groh, A. Pirrera, M. Schenk, Shape control for experimental continuation. *Phys. Rev. Lett.* **120**, 254101 (2018).
38. N. P. Bende, A. A. Evans, S. Innes-Gold, L. A. Marin, I. Cohen, R. C. Hayward, C. D. Santangelo, Geometrically controlled snapping transitions in shells with curved creases. *Proc. Natl. Acad. Sci. U.S.A.* **112**, 11175–11180 (2015).
39. J. R. Raney, N. Nadkarni, C. Daraio, D. M. Kochmann, J. A. Lewis, K. Bertoldi, Stable propagation of mechanical signals in soft media using stored elastic energy. *Proc. Natl. Acad. Sci. U.S.A.* **113**, 9722–9727 (2016).

40. N. Nadkarni, A. F. Arrieta, C. Chong, D. M. Kochmann, C. Daraio, Unidirectional transition waves in bistable lattices. *Phys. Rev. Lett.* **116**, 244501 (2016).
41. S. Shan, S. H. Kang, J. R. Raney, P. Wang, L. Fang, F. Candido, J. A. Lewis, K. Bertoldi, Multistable architected materials for trapping elastic strain energy. *Adv. Mater.* **27**, 4296–4301 (2015).
42. T. Chen, O. R. Bilal, K. Shea, C. Daraio, Harnessing bistability for directional propulsion of soft, untethered robots. *Proc. Natl. Acad. Sci. U.S.A.* **115**, 5698–5702 (2018).
43. A. Rafsanjani, A. Akbarzadeh, D. Pasini, Snapping mechanical metamaterials under tension. *Adv. Mater.* **27**, 5931–5935 (2015).

Funding: Research was supported by the NSF grants DMR-1420570 and DMR-1922321 and the Fund for Scientific Research-Flanders (FWO). **Author contributions:** B.G. proposed the research idea. B.G., D.M., N.V., M.T., and K.B. developed the concept and designed the research. D.M. conducted the numerical simulations. B.G. fabricated the prototypes. B.G. and D.M. performed the experiments. B.G., D.M., and K.B. postprocessed the data and wrote the paper. K.B. supervised the research. **Competing interests:** The authors declare that they have no competing interests. **Data and materials availability:** All data needed to evaluate the conclusions in the paper are present in the paper or the Supplementary Materials.

Submitted 6 February 2020
Accepted 8 April 2020
Published 20 May 2020
10.1126/scirobotics.abb1967

Citation: B. Gorissen, D. Melancon, N. Vasios, M. Torbati, K. Bertoldi, Inflatable soft jumper inspired by shell snapping. *Sci. Robot.* **5**, eabb1967 (2020).

Science Robotics

Inflatable soft jumper inspired by shell snapping

Benjamin Gorissen, David Melancon, Nikolaos Vasios, Mehdi Torbati and Katia Bertoldi

Sci. Robotics **5**, eabb1967.
DOI: 10.1126/scirobotics.abb1967

Science Robotics
AAAS

robotics.sciencemag.org/cgi/content/full/5/42/eabb1967/DC1

Supplementary Materials for

Inflatable soft jumper inspired by shell snapping

Benjamin Gorissen, David Melancon, Nikolaos Vasios, Mehdi Torbati, Katia Bertoldi*

*Corresponding author. Email: bertoldi@seas.harvard.edu

Published 20 May 2020, *Sci. Robot.* **5**, eabb1967 (2020)
DOI: 10.1126/scirobotics.abb1967

The PDF file includes:

Section S1. Design
Section S2. Fabrication
Section S3. Testing
Section S4. FE simulations
Section S5. Mass-spring model to predict the jump height
Section S6. Additional results
Fig. S1. Ideal design of the inflatable actuators.
Fig. S2. Manufacturable design of the inflatable actuators.
Fig. S3. Fabrication of the inflatable actuators.
Fig. S4. Baseline designs of the inflatable actuators.
Fig. S5. Experimental setup of the inflation with water.
Fig. S6. Experimental pressure-volume curves of the inflatable actuators.
Fig. S7. Experimental setup of the inflation with air.
Fig. S8. Jumping tests of the inflatable actuators.
Fig. S9. Effect of air compressibility.
Fig. S10. Numerical and experimental pressure-volume curves of the inflatable actuators.
Fig. S11. Pole displacement of the inflatable actuators.
Fig. S12. Three-dimensional simulations of the inflatable actuators.
Fig. S13. Axisymmetric simulations of the inflatable actuators.
Fig. S14. Extracting ΔE from the numerical p-v curves.
Fig. S15. Axisymmetric simulations of the inner cap.
Fig. S16. Asymmetric deformation emerges in designs with self-crossing pressure-volume curves.
Fig. S17. Axisymmetric simulations of the outer cap.
Fig. S18. Mass-spring model to predict jump height.
Fig. S19. Jump height prediction of the inflatable actuators.
Fig. S20. Validation of the spring-mass model.
Fig. S21. Improving the performance our soft fluidic actuators through a grid search.
Fig. S22. Influence of the outer cap stiffness on the actuators' response.

Legends for movies S1 to S6

Other Supplementary Material for this manuscript includes the following:

(available at robotics.sciencemag.org/cgi/content/full/5/42/eabb1967/DC1)

Movie S1 (.avi format). Snapping of spherical caps results in a sudden release of elastic energy.
Movie S2 (.avi format). Fast fluidic soft robots inspired by shell snapping.
Movie S3 (.avi format). Isochoric snapping enables jumping in fluidic soft robots.
Movie S4 (.avi format). Simplified mass-spring model to predict jump height.
Movie S5 (.avi format). Improving jumper design to increase jump height.
Movie S6 (.avi format). Inflatable actuator with repetitive jumping.

Section S1. Design

Our fluidic actuators are made out of two spherical caps: an inner cap that buckles under internal positive pressure and an outer cap that stretches under the same internal positive pressure. In this Section, we first describe the ideal design in which the two caps are connected through a single line contact and then detail the modifications introduced to facilitate their fabrication. Note that throughout this manuscript, we will use the subscripts i and o to indicate the inner and outer caps, respectively.

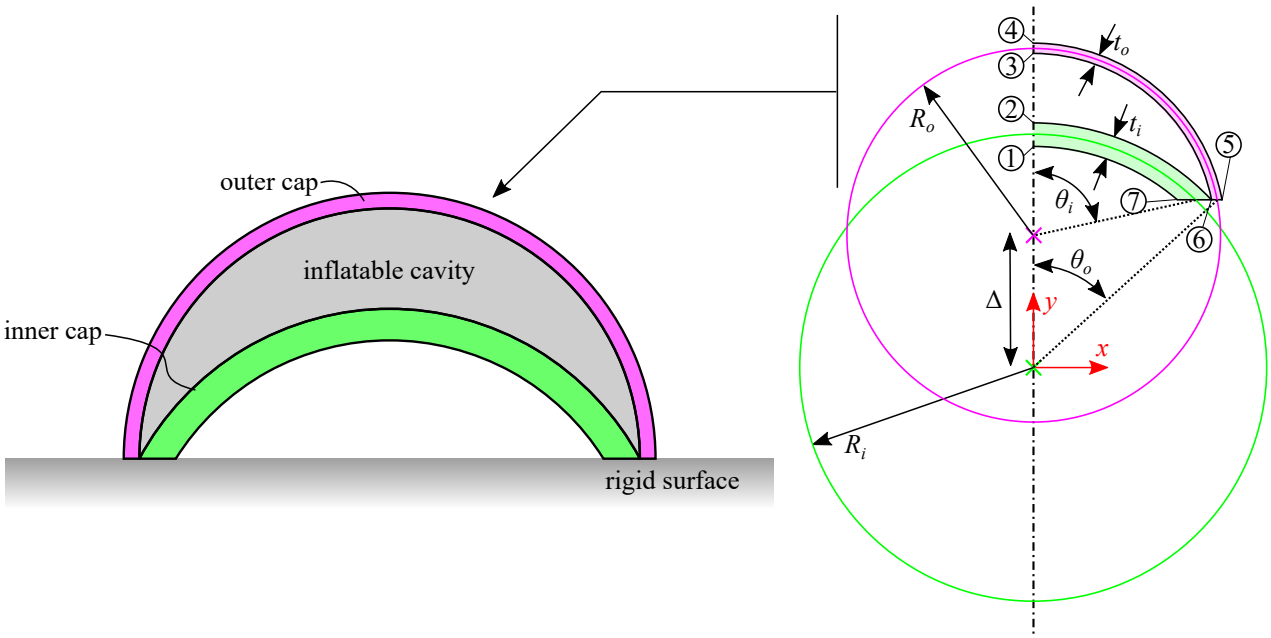

Fig. S1. Ideal design of the inflatable actuators. Schematics of the ideal design highlighting the seven points of the axisymmetric cross-section.

A. Ideal design. As shown in Fig. S1, our actuators consist of two axisymmetric spherical caps. As such, their geometry is fully defined by the opening angles θ_i and θ_o, the radii of the spheres R_i and R_o, the cap thicknesses t_i and t_o, and the center-to-center distance between the two spheres, Δ. More specifically, the coordinates of the seven points indicated in Fig. S1, which define the cross section of the actuator are given by

$$(x_1, y_1) = \left(0, R_i\left(1 - \frac{1}{2\eta_i}\right)\right) \tag{1a}$$

$$(x_2, y_2) = \left(0, R_i\left(1 + \frac{1}{2\eta_i}\right)\right) \tag{1b}$$

$$(x_3, y_3) = \left(0, R_o\left(1 - \frac{1}{2\eta_o}\right) + \Delta\right) \tag{1c}$$

$$(x_4, y_4) = \left(0, R_o\left(1 + \frac{1}{2\eta_o}\right) + \Delta\right) \tag{1d}$$

$$(x_5, y_5) = \left(R_o\sqrt{\left(1 + \frac{1}{2\eta_o}\right)^2 - \cos^2(\theta_o)}, R_i\cos(\theta_i)\right) \tag{1e}$$

$$(x_6^i, y_6^i) = \left(R_i\sqrt{\left(1 + \frac{1}{2\eta_i}\right)^2 - \cos^2(\theta_i)}, R_i\cos(\theta_i)\right) \tag{1f}$$

$$(x_6^o, y_6^o) = \left(R_o\sqrt{\left(1 - \frac{1}{2\eta_o}\right)^2 - \cos^2(\theta_o)}, R_o\cos(\theta_o) + \Delta\right) \tag{1g}$$

$$(x_7, y_7) = \left(R_i\sqrt{\left(1 - \frac{1}{2\eta_i}\right)^2 - \cos^2(\theta_i)}, R_i\cos(\theta_i)\right), \tag{1h}$$

[1i]

where $\eta_i = R_i/t_i$ and $\eta_o = R_o/t_o$ are the normalized radii, and (x_6^i, y_6^i) and (x_6^o, y_6^o) are the coordinates of point 6 expressed in terms of the inner cap and outer cap, respectively. However, an inflatable cavity is formed only if

$$x_6^i = x_6^o, \quad \text{and} \quad y_6^i = y_6^o \tag{2}$$

and we solve these two equations by substituting equations [1f] and [1g] to express the radius of the outer cap, R_o, and the center-to-center distance between the spheres, Δ, as a function of the other parameters:

$$R_o = R_i \sqrt{\frac{\left(1+\frac{1}{2\eta_i}\right)^2 - \cos^2(\theta_i)}{\left(1-\frac{1}{2\eta_o}\right)^2 - \cos^2(\theta_o)}}, \tag{3a}$$

$$\Delta = R_i \left(\cos(\theta_i) - \cos(\theta_o) \sqrt{\frac{\left(1+\frac{1}{2\eta_i}\right)^2 - \cos^2(\theta_i)}{\left(1-\frac{1}{2\eta_o}\right)^2 - \cos^2(\theta_o)}} \right). \tag{3b}$$

It follows that the geometry of the actuators is fully defined by 4 dimensionless and independent parameters:

$$\theta_i, \quad \theta_o, \quad \eta_i = \frac{R_i}{t_i}, \quad \eta_o = \frac{R_o}{t_o}. \tag{4}$$

Further, in order for the two caps to not intersect, we need to respect the following inequality constraints:

$$\begin{aligned} \theta_i &< \theta_o, \\ y_2 &< y_3. \end{aligned} \tag{5}$$

B. Modifications to facilitate fabrication. As shown in Fig. S1, the inner and outer caps are only connected through a line contact, which provides no structural integrity. To this end, we modify the geometry to enhance the robustness of the actuator, but also facilitate its fabrication. In particular, we extend the inner cap by introducing a ring around its base with thickness t_{ring} and width w_{ring} (see Fig. S2). As such, the base of the inner cap's cross section is defined by the three vertices:

$$(x_8, y_8) = \left(R_i \sqrt{\left(1-\frac{1}{2\eta_i}\right)^2 - \cos^2(\theta_i)}, R_i \left(\cos(\theta_i) - \frac{1}{\bar{t}_{ring}} \right) \right) \tag{6a}$$

$$(x_9, y_9) = \left(R_i \left(\sqrt{\left(1+\frac{1}{2\eta_i}\right)^2 - \cos^2(\theta_i)} + \frac{1}{\bar{w}_{ring}} \right), R_i \left(\cos(\theta_i) - \frac{1}{\bar{t}_{ring}} \right) \right) \tag{6b}$$

$$(x_{10}, y_{10}) = \left(R_i \left(\sqrt{\left(1+\frac{1}{2\eta_i}\right)^2 - \cos^2(\theta_i)} + \frac{1}{\bar{w}_{ring}} \right), R_i \cos(\theta_i) \right), \tag{6c}$$

[6d]

where $\bar{t}_{ring} = R_i/t_{ring}$ and $\bar{w}_{ring} = R_i/w_{ring}$.

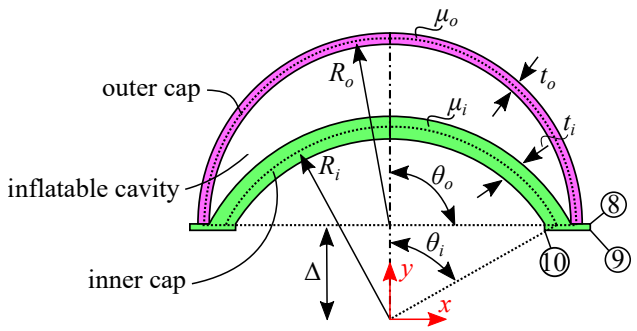

Fig. S2. Manufacturable design of the inflatable actuators. Schematic of the design with the modifications made to facilitate fabrication.

Section S2. Fabrication

The actuators tested in this study are made of nearly incompressible silicone rubbers. Specifically, we use both Elite Double 32 from Zhermack (with green color and initial shear modulus $\mu = 0.35$ MPa) and Elite Double 8 from Zhermack (with purple color and initial shear modulus $\mu = 0.06$ MPa). The two caps are casted with a two-part mold, which is designed using NX 12 (Siemens) and 3d printed in VeroClear with a Connex3 Objet500 printer (Stratasys). The inner cap and outer cap are molded separately and combined afterwards to form an enclosed, inflatable cavity. Specifically, our actuators are fabricated using the following 12 steps (see Fig. S3):

- **Step 1:** we coat all inner mold surfaces with a release agent (Ease Release 200 spray, Mann Release Technologies) to facilitate demolding in a later step.
- **Step 2:** we fill the bottom halves of the molds with uncured polymer. In the case shown in Fig. S3, we use Elite Double 32 (Zhermack) for the inner cap and Elite Double 8 (Zhermack) for the outer cap.
- **Step 3:** we close both molds with pressure clamps to ensure accurate layer thickness and wait 15 minutes for the polymer to cure.
- **Step 4:** we remove both cured caps from the molds.
- **Step 5:** we puncture the outer cap to create an access hole for a tube.
- **Step 6:** we insert the tube in the outer cap.
- **Step 7:** we apply glue (Sil-Poxy Silicone Adhesive - Smooth-On) around the edges of the top surface of the ring at the base of the inner cap.
- **Step 8:** we connect the outer cap to the inner cap and wait 15 minutes for the glue to cure.
- **Step 9:** we apply glue (Sil-Poxy Silicone Adhesive -Smooth-On) to fix the tube to the outer cap.
- **Step 10:** we wait 15 minutes for the glue to cure.
- **Step 11:** we connect the actuator to a syringe pump.
- **Step 12:** we inflate the actuator to make sure there are no leaks.

As part of this study, we fabricate four prototypes, all with $R_i = 30$mm, $\bar{t}_{ring} = \frac{R_i}{t_{ring}} = 30$, $\bar{w}_{ring} = \frac{R_i}{w_{ring}} = 10$, and (see Fig. S4)

- *Design A:* $\eta_i = 30$, $\eta_o = 16.5$, $\theta_i = 60^\circ$, $\theta_o = 90^\circ$ and $\mu_i/\mu_o = 1$;
- *Design B:* $\eta_i = 8.5$, $\eta_o = 16.5$, $\theta_i = 60^\circ$, $\theta_o = 90^\circ$ and $\mu_i/\mu_o = 1$;
- *Design C:* $\eta_i = 8.5$, $\eta_o = 16.5$, $\theta_i = 60^\circ$, $\theta_o = 90^\circ$ and $\mu_i/\mu_o = 5.8$;
- *Design D:* $\eta_i = 6.2$, $\eta_o = 12.1$, $\theta_i = 80^\circ$, $\theta_o = 82^\circ$ and $\mu_i/\mu_o = 5.8$;

where μ_i/μ_o is the ratio between the initial shear modulus of the rubber used to fabricate the inner and outer caps, respectively.

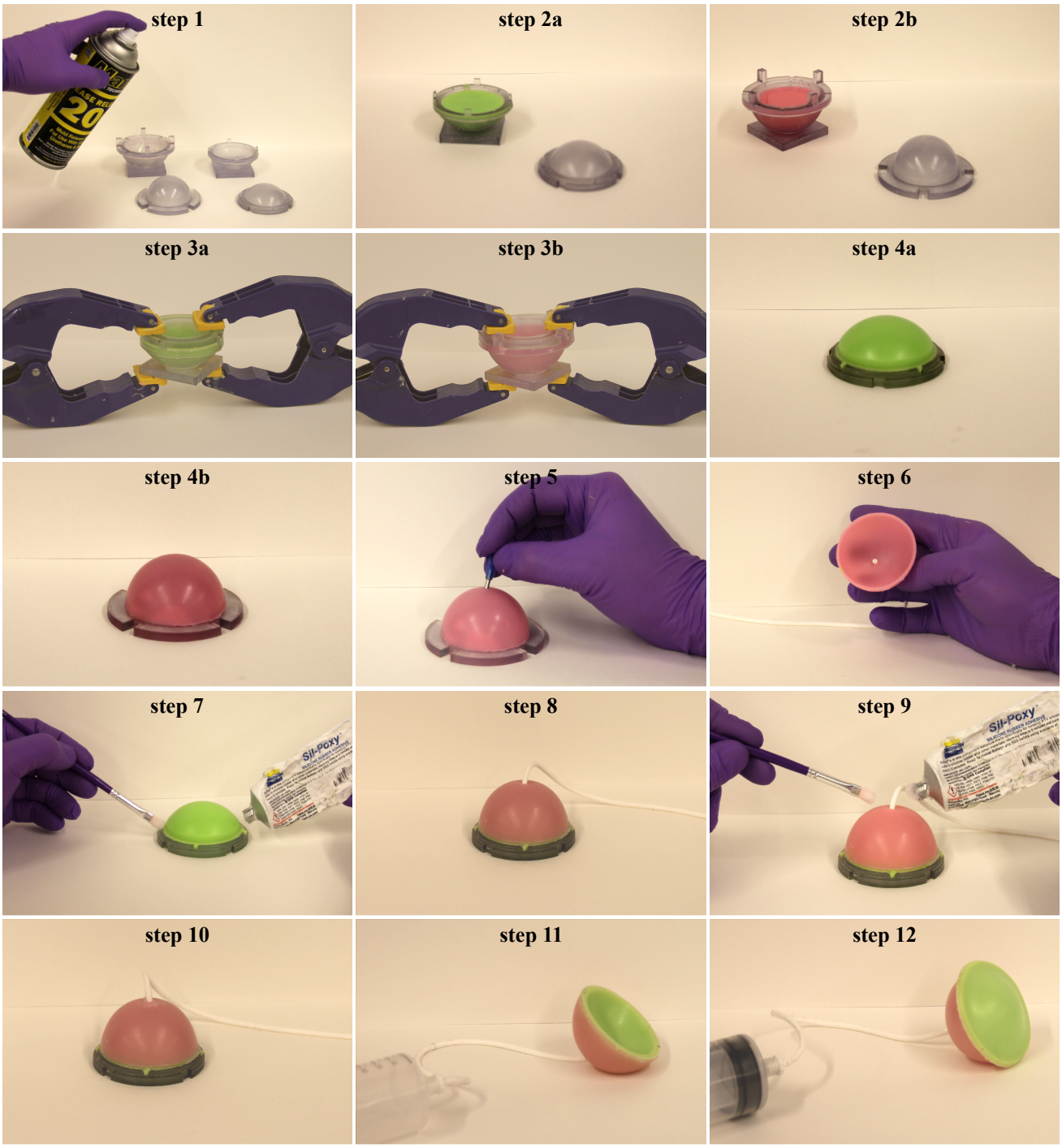

Fig. S3. Fabrication of the inflatable actuators. Snapshots of the 12 steps required to fabricate our actuators

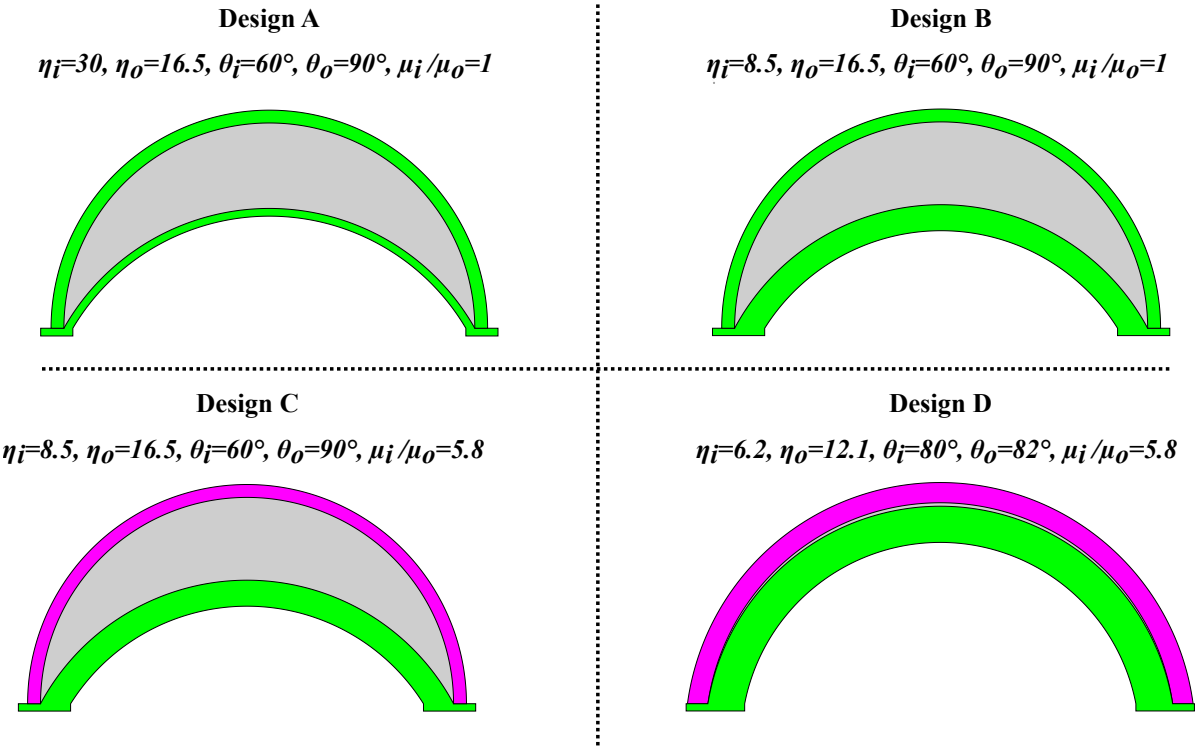

Fig. S4. Baseline designs of the inflatable actuators. Schematics of the four designs fabricated as part of this study.

Section S3. Testing

In order to fully characterize the response of the fabricated actuators under quasi-static inflation, we first inflate them with water to measure their pressure-volume relation and then with air to assess their ability to jump.

A. Inflation with water. First, to decouple the effect of the geometry of the actuators from that of the compressibility of the fluid, we determine the pressure-volume curve by inflating the actuators with water. As depicted in Fig. S5, we use a syringe pump (Pump 33DS, Harvard Apparatus) to displace water into the actuator at 10 mL/min and measure the pressure using a pressure sensor (MPXV7002DP with a measurement range of ±2 kPa and MPXV7025DP with a measurement range of ±25 kPa, both by NXP USA). Note that to eliminate the influence of gravity, we submerge the entire actuator in a water tank. Moreover, to accurately determine the pressure-volume relation, air is eliminated from all supply tubes and the pressure is calibrated to atmospheric pressure before each measurement cycle.

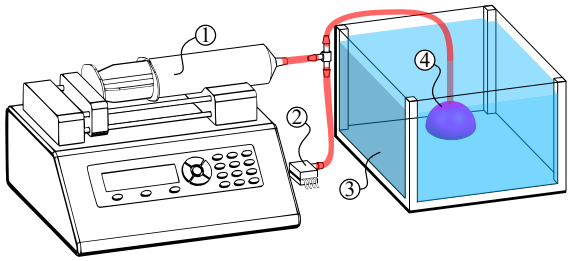

Fig. S5. Experimental setup of the inflation with water. Schematic of the test setup used to characterize the pressure-volume characteristic of the prototype actuators. (1) Syringe pump. (2) Pressure sensor. (3) Water tank. (4) Actuator.

In Fig. S6, we report the experimentally measured pressure-volume curves for Designs A-D, with the blue lines corresponding to inflation and the red ones to deflation. To make sure the response is repeatable, for each design we test three specimens across three inflation-deflation cycles. The continuous lines correspond to the mean of the responses recorded in all tests and the shaded region to the standard deviation.

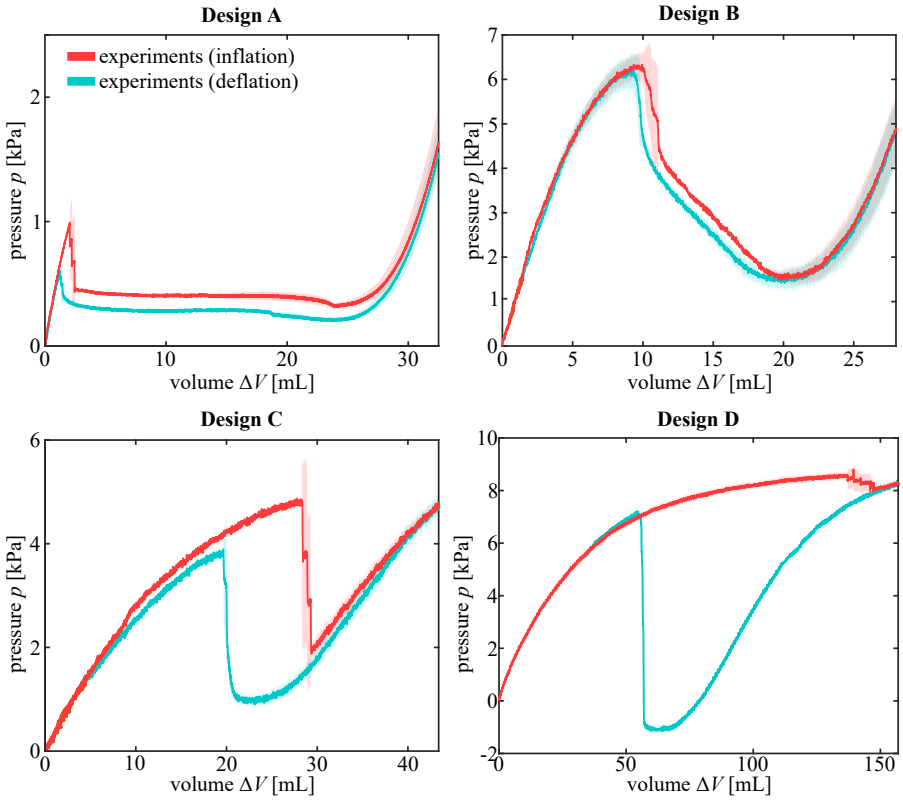

Fig. S6. Experimental pressure-volume curves of the inflatable actuators. Pressure vs. volume relationships measured for Designs A-D. The shaded region represents the standard deviation obtained from testing three specimens for each geometry.

B. Inflation with air. To investigate how snapping can be exploited to make our actuators jump even when inflated at a slow rate, we position them on a flat surface (to minimize the effect of viscous forces) and slowly inflate them with air (to minimize the effect of gravity). Specifically, we inflate them with air at 10 mL/min using a syringe pump (Pump 33DS, Harvard Apparatus), while capturing their deformation with a high speed camera (SONY RX100 V) recording at 240 frames per second (see Fig. S7). The jump height, y_{jump}, is defined as the distance between the flat surface and the lowest point of the inner cap measured when the actuator reaches its highest point (see Fig. S9). In Fig. S8, we show frames extracted from the recorded movies for the four different designs that we fabricated as part of this study. We find that only Designs C and D are able to jump and that $y_{jump} = 42.9$ mm and 283 mm for Design C and Design D, respectively.

Finally, we note that, although this last set of test was conducted using a compressible fluid (air), the effect of fluid compressibility on the response of the system energy release is negligible. To demonstrate this important point, we also measure the pressure-volume curve of Design C while inflating with air at 10 mL/min and taking into account its compressibility to measure the volume inside the actuator. Specifically, the current volume of the system (which comprises the actuator, syringe, and connecting tube), V, at a given pressure p can be expressed as,

$$V = V_0^{sys} + \Delta V - \Delta V^{\text{syringe}}, \qquad [7]$$

where V_0^{sys} is the initial pressure and volume of the system (which comprises the actuator, syringe, and connecting tube), ΔV is the change in volume of the actuator and $\Delta V^{\text{syringe}}$ is the amount of volume dispense by the syringe. Since our system is a closed one

$$p_0 V_0^{sys} = pV, \qquad [8]$$

which we combine with Eq. (7) to obtain

$$\Delta V = \Delta V^{\text{syringe}} - \left(\frac{p - p_0}{p}\right) V_0^{sys}. \qquad [9]$$

where p_0 is the initial pressure of the system. Given the fast time-scale of snapping, we can assume that during the instability $\Delta V^{\text{syringe}}$ is constant. Then, it follows that the change in volume of the actuator during snapping is

$$\Delta V^+ - \Delta V^- = \left(\frac{p^+ - p_0}{p^+} - \frac{p^- - p_0}{p^-}\right) V_0^{sys} = \frac{p_0(p^+ - p^-)}{p^+ p^-} V_0^{sys}, \qquad [10]$$

where the superscripts $-$ and $+$ are used to indicate quantities evaluated immediately before and after snapping, respectively. Eq. (10) reveals that the drop in pressure that accompanies snapping results in a change in the volume of the actuator that scales with the initial volume V_0^{sys}.

In Fig. S9 we report the pressure-volume curves for Design C as measured in three different tests in which we vary the initial volume of air in the syringe (so that V_0^{sys}=40, 45 and 100 ml). We find that in all three cases the response of the actuator is close to that measured when inflating with air.

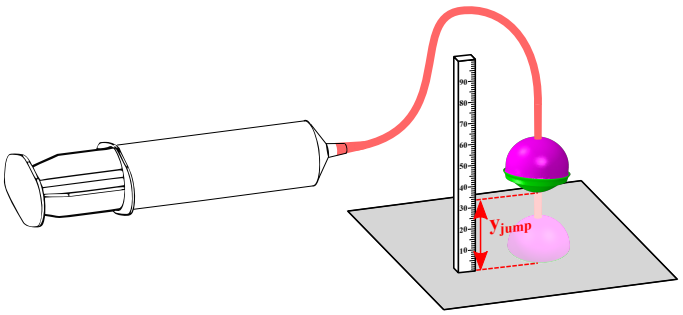

Fig. S7. Experimental setup of the inflation with air. Schematic of the test setup used to characterize the ability of the actuators to jump.

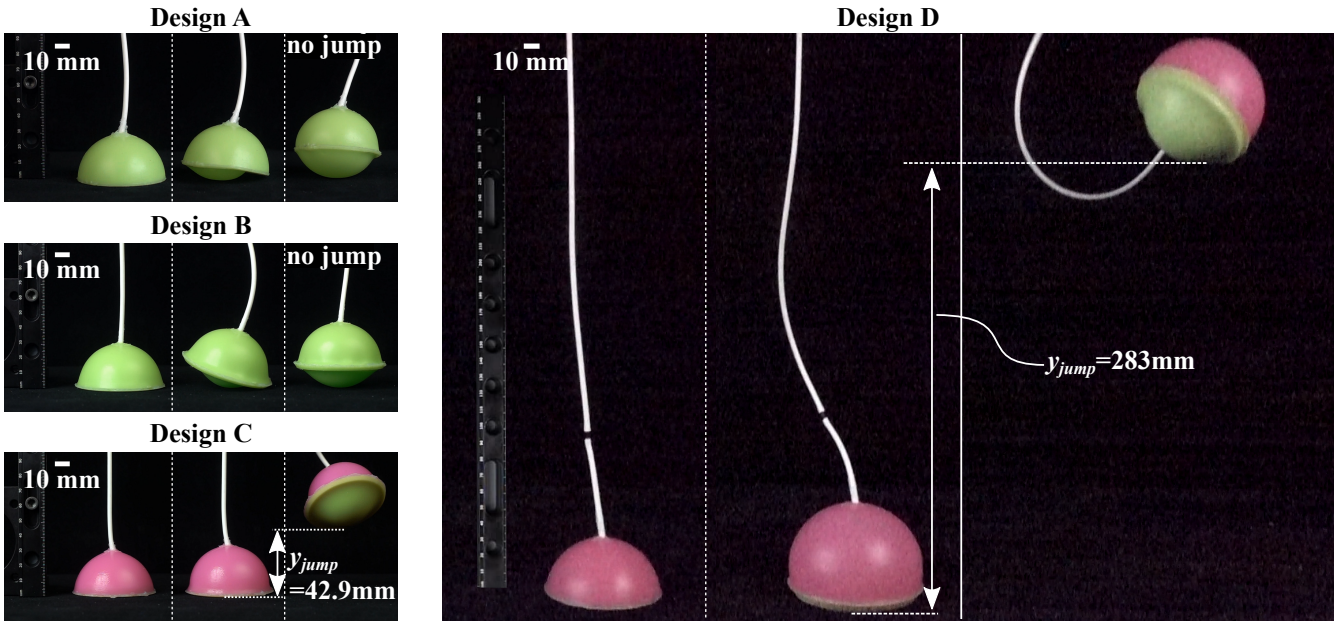

Fig. S8. Jumping tests of the inflatable actuators. Snapshots of the actuators before inflation, just before snapping of the inner cap, and at their highest point.

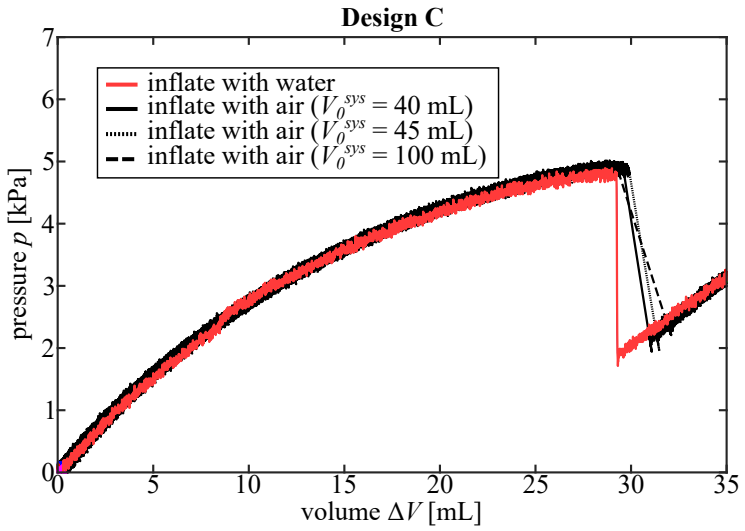

Fig. S9. Effect of air compressibility. Pressure vs. volume relationships measured for Design C inflated with water and air for three different tests in which we vary V_0^{sys} by controlling the initial volume of air in the syringe.

Section S4. FE simulations

To gain a deeper understanding of the mechanical response of the inflatable actuators and calculate their release of energy and pole displacement during snapping, we perform Finite Element (FE) simulations using the commercial package ABAQUS 2018/Standard. In all our analyses, the response of the silicone rubber used to fabricate the caps (Elite Double 32 and Elite Double 8 from Zhermack) is modeled using an incompressible Gent material model [17] with strain energy density function W given by

$$W = -\frac{\mu J_{lim}}{2} \ln\left(1 - \frac{I_1 - 3}{J_{lim}}\right), \qquad [11]$$

where μ and J_{lim} represent the small strain shear modulus and a material parameter related to the limiting stretch, respectively, and $I_1 = \mathrm{tr}(\mathbf{F}^T\mathbf{F})$, $\mathbf{F}$ being the deformation gradient. We find that the response of the pink Elite Double 8 and the green Elite Double 32 is accurately captured using (μ, J_m) = (0.06 MPa, 24) and (0.35 MPa, 24), respectively. Note that these values are obtained by minimizing the error between experiments and simulations for Design C and that the obtained values for the shear modulus are within the range previously reported in the literature [21,23-25]. An in-house ABAQUS user subroutine (UHYPER) is used to define the hyperelastic material behavior given by Eq. [11] in the FE simulations.

In the following, we present the different types of simulations used to determine the behavior off the actuator upon quasi-satic inflation.

A. 3D simulations. We start by conducting full 3D FE simulations of the actuators. To this end, we create 3D models and discretize them using a non-structured mesh of 4-node linear tetrahedron elements (ABAQUS element type: C3D4H), with mesh size adapted to ensure that at least four elements are used to discretize the thickness of the thinnest cap.

To remove rigid body translations and rotations, we impose a no vertical displacement boundary condition ($u_y = 0$) at the nodes located on the line of contact between the two caps (defined by point 6 in Fig. S1). All models are inflated via a fluid cavity interaction with an hydraulic fluid (of density $\rho = 1000$ kg/m^3 and bulk modulus $B = 2000$ MPa). The volume-controlled inflation is driven by a fictitious thermal expansion of the hydraulic fluid, relating to the change in volume ΔV in the cavity through,

$$\frac{\Delta V}{V_0^{cav}} = 3\alpha_T \Delta T, \qquad [12]$$

where ΔT is the change in temperature, α_T is the coefficient of thermal expansion of the fluid and V_0^{cav} is the initial volume of the cavity. In the simulations, we set $\alpha_T = 1$ m/(m$\cdot$ K) and gradually increase the temperature ΔT until the isochoric snap-through is reached. We simulate the inflation using the dynamic implicit solver (using a density of $\rho = 1000$ kg/m^3 for the silicone rubber) and ensure quasi-static conditions by monitoring the kinetic energy of the model (note that quasi-static conditions are achieved by using a time period of 1 second, minimum increment size of 1e$-$10 s, maximum increment size of 0.01 s, and $10,000$ maximum number of increments).

In Figs. S10, S11, and S12 we report the pressure vs. volume curves, pole displacement vs. volume relations, and numerical snapshots of the deformed configurations for Designs A-D. First, in Fig. S10, we find very good agreement between the pressure-volume curve measured in experiments and predicted by our simulations, with the numerical analyses that correctly capture the isochoric snap-through instability. Second, in in Fig. S11, the numerical predictions for the evolution of the pole displacement of Designs C and D suggest that the snap-through instability is accompanied by a sudden and large change in the displacement of the pole, which ultimately enables these Designs to jump. Finally, by looking at the deformation experienced by the actuators during inflation and deflation (Fig. S12), we find that Designs C and D maintain an axisymmetric configurations also during the isochoric snap-through.

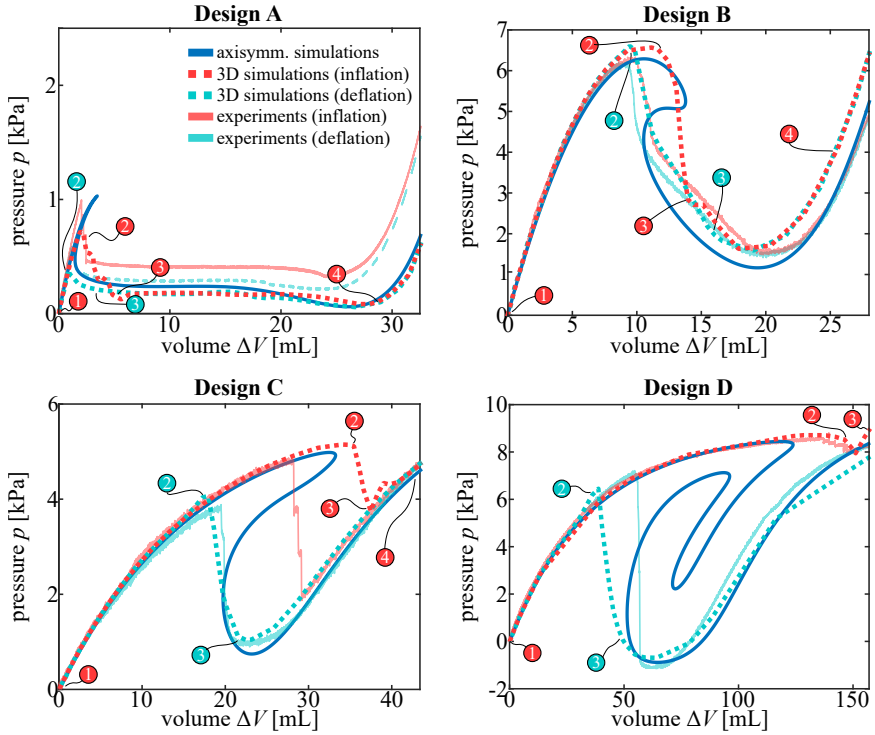

Fig. S10. Numerical and experimental pressure-volume curves of the inflatable actuators. Pressure-volume relations for Designs A-D as predicted by our 3D (blue dashed lines for inflation and orange dashed lines for deflation) and axisymmetric (black line) simulations and measured in experiments (blue solid lines for inflation and orange solid lines for deflation). The numbers on the plots indicate the deformation states shown in Fig. S10.

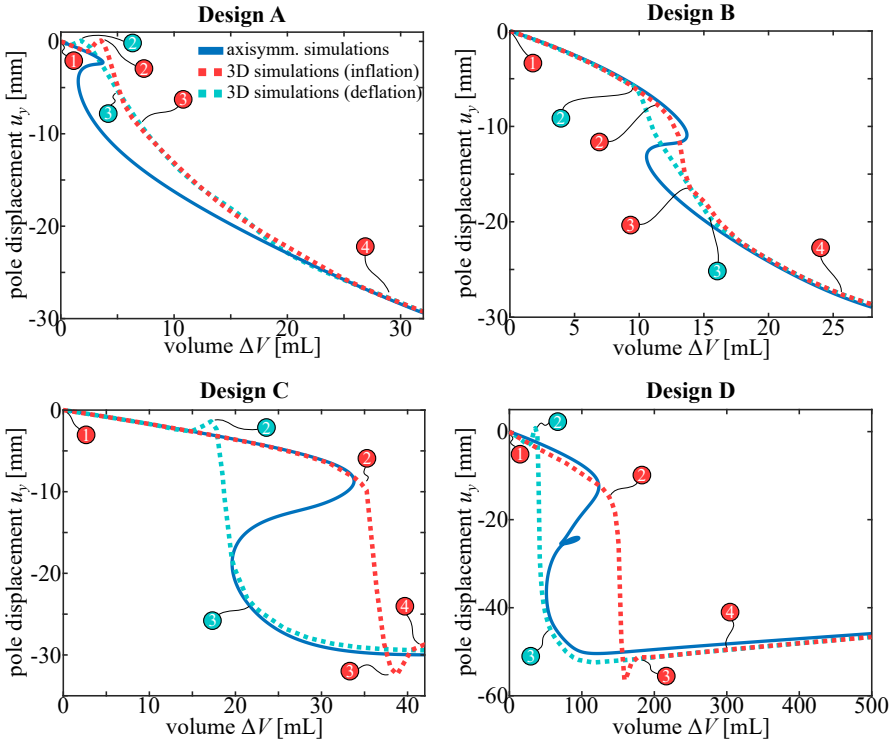

Fig. S11. Pole displacement of the inflatable actuators. Pole displacement vs. volume curves for Designs A-D as predicted by our 3D (blue dashed lines for inflation and orange dashed lines for deflation) and axisymmetric (black line) simulations. The numbers on the plots indicate the deformation states shown in Fig. S12.

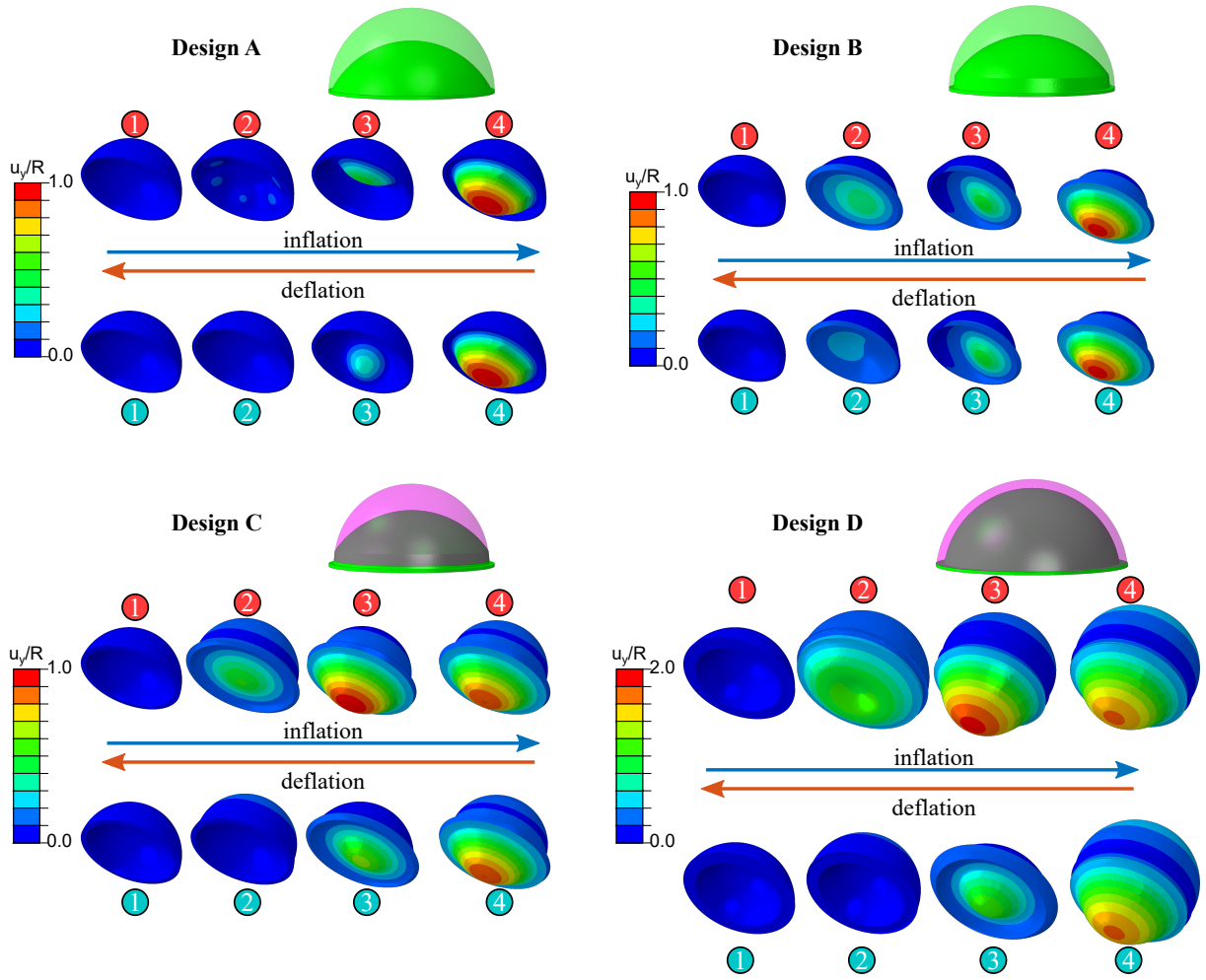

Fig. S12. Three-dimensional simulations of the inflatable actuators. Numerical snapshots showing the deformation of Designs A-D as predicted by our 3D FE simulations for inflation and deflation. The numbers next to the snapshots correspond to the numbers indicated in Figs. S10 and S11.

B. Axisymmetric simulations. While our 3D FE simulations accurately capture and predict the response of our actuators, their high computational cost prohibits their use for efficient exploration of the design space. To this end, we assume that the deformation of the actuators is axisymmetric and discretize the models using using 4-node bilinear axisymmetric solid elements (ABAQUS element type: CAX4H), with the mesh size adapted to make sure the thinnest cap has at least four elements through thickness. To predict the energy released during the isochoric snap-through, we determine the full pressure-volume relation using the modified Riks algorithm [18-19] as implemented in Abaqus. As for the 3D simulations, the axisymmetric models are inflated via a fluid cavity interaction with an hydraulic fluid (of density $\rho = 1000$ kg/m^3 and bulk modulus $B = 2000$ MPa) and we stop inflating when the pressure p is equal to

$$p = 1.5\, p_c, \qquad [13]$$

where p_c is the critical pressure for a thin spherical shell and the factor 1.5 is introduced to account for the fact that most of the caps we are simulating are not thin (i.e. $R/t < 25$). For a spherical shell of radius R and thickness t, such critical pressure can be estimated as [22]

$$p_c = \frac{2E}{\sqrt{3(1-\nu^2)}} \left(\frac{t}{R}\right)^2, \qquad [14]$$

where E and ν are the Young's modulus and Poisson's ratio, respectively (for the considered incompressible hyperelastic material $E = 3\mu$ and $\nu = 0.5$).

Full actuators. To simulate the response of the actuators, we impose roller boundary conditions ($u_x = 0$) on the rotational axis of symmetry. Moreover, to eliminate rigid-body translations and rotations, we impose a no vertical displacement boundary condition at the point of contact between the two caps (Fig. S13A). In Fig. S13, we focus on Design C and report numerical snapshots at different levels of inflation (Fig. S13B), the pressure-volume curve (Fig. S13C), the evolution of the strain energy as a function of volume (Fig. S13D), and the evolution of the pole displacement as a function of volume (Fig. S13E) as

predicted by our axisymmetric simulations. Since the Riks analyses is able to trace the entire pressure-volume curve, we can direcly extract the energy released ΔE during the isochoric snap-through (see highlighted area in blue in Fig. S13C and step-by-step method in Fig. S14). Moreover, in Figs. S11 and S13 we compare the numerical predictions of our axisymmetric analyses with those of the 3D simulations. The good agreement between the two sets of data validates the axisymmetric analyses.

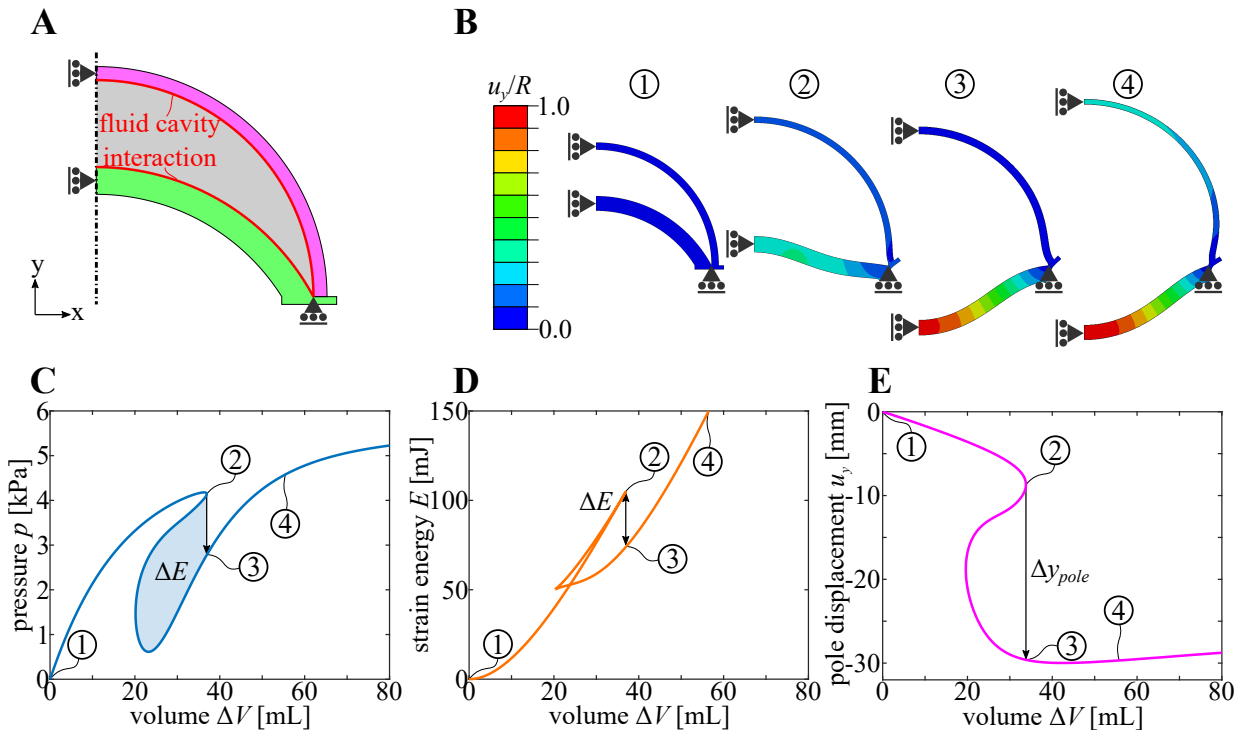

Fig. S13. Axisymmetric simulations of the inflatable actuators. A. Schematic of the axisymmetric model. **B.** Numerical snapshots of Design C at (1) rest, (2) before snapping, (3) after snapping, and (4) upon further inflation. **C.** Pressure vs. volume relation as predicted by our axisymmetric simulations for Design C. **D.** Strain energy vs. volume relation as predicted by our axisymmetric simulations for Design C. **E.** Pole displacement vs. volume relation as predicted by our axisymmetric simulations for Design C.

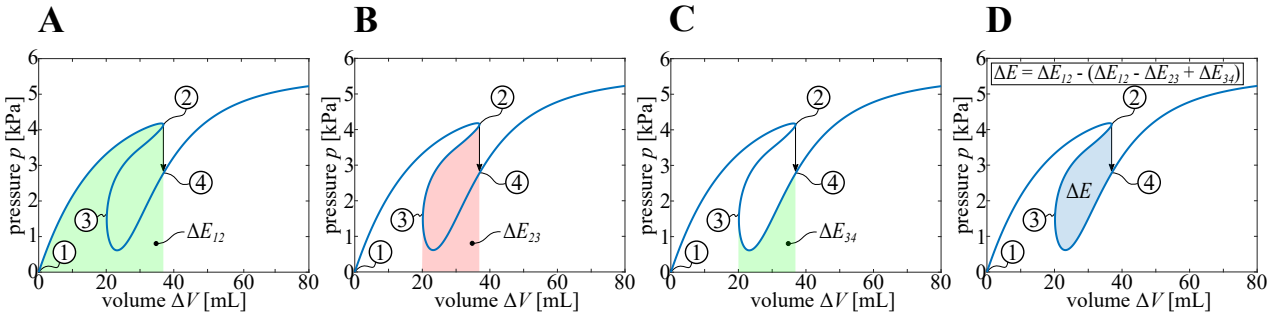

Fig. S14. Extracting ΔE from the numerical p-v curves of the full actuators. A. Highlighted green region represents the strain energy stored in the system when inflated up to the snapping point (i.e. when inflated from state (1) to state (2)). **B.** Highlighted red region represents the strain energy released from the system when it moves from state (2) to state (3). **C.** Highlighted green region represents the strain energy stored in the system between when it moves from state (3) to state (4). **D.** Highlighted blue region represents the energy released from the system during the isochoric snap-through.

Separate inner and outer caps. To gain further insights into the response of our actuators, we investigate separately the inner and the outer caps via axisymmetric simulations for a wide range of geometric parameters (i.e.$40^\circ \leq \theta_i \leq 80^\circ$, $5 \leq \eta_i \leq 12.5$, $40^\circ \leq \theta_o \leq 90^\circ$, $5 \leq \eta_o \leq 20$). Similarly to the actuator, the models in these cases are discretized with 4-node bilinear axisymmetric solid elements (CAX4H element type) with mesh size adapted to ensure at least four elements through thickness. For both inner and outer caps, we capture the materials response using the Gent model (Eq. [11]) and impose $u_x = 0$ on the rotational axis of symmetry. Moreover, for the inner cap we impose $u_y = 0$ at the connection between the base of the cap and the angular ring (inset in Fig. S15F), whereas for the outer cap we assume that the base is completely fixed (Fig. S17B).

Focusing on the inner cap, the numerical results summarized in Fig. S15A-B indicate that by varying the polar angle θ_i and the radius to thickness ratio η_i, the response of the cap undergoes several transitions. For low values of θ_i and η_i (i.e. for thick and shallow caps), the inner cap does not exhibit the snap-through behavior (see light grey region in Fig. S15B-C). By increasing θ_i at constant η_i, a snap-through instability is eventually triggered upon inflation, which results in a sudden release of energy and fast cap's pole displacement. Within this domain, ΔE_i and Δy_{pole} both increase monotonically as a function of θ_i (see Fig. S15C). Finally, for high values of θ_i and η_i (i.e. for thin and deep caps) the pressure-volume curves become self-crossing (see dark grey region in Fig. S15-B). By comparing the results of axisymmetric and 3D simulations we find that a highly complex, self-crossing pressure-volume response indicates the existence of a more favorable asymmetric deformation path with low energy release upon snapping (Fig. S16).

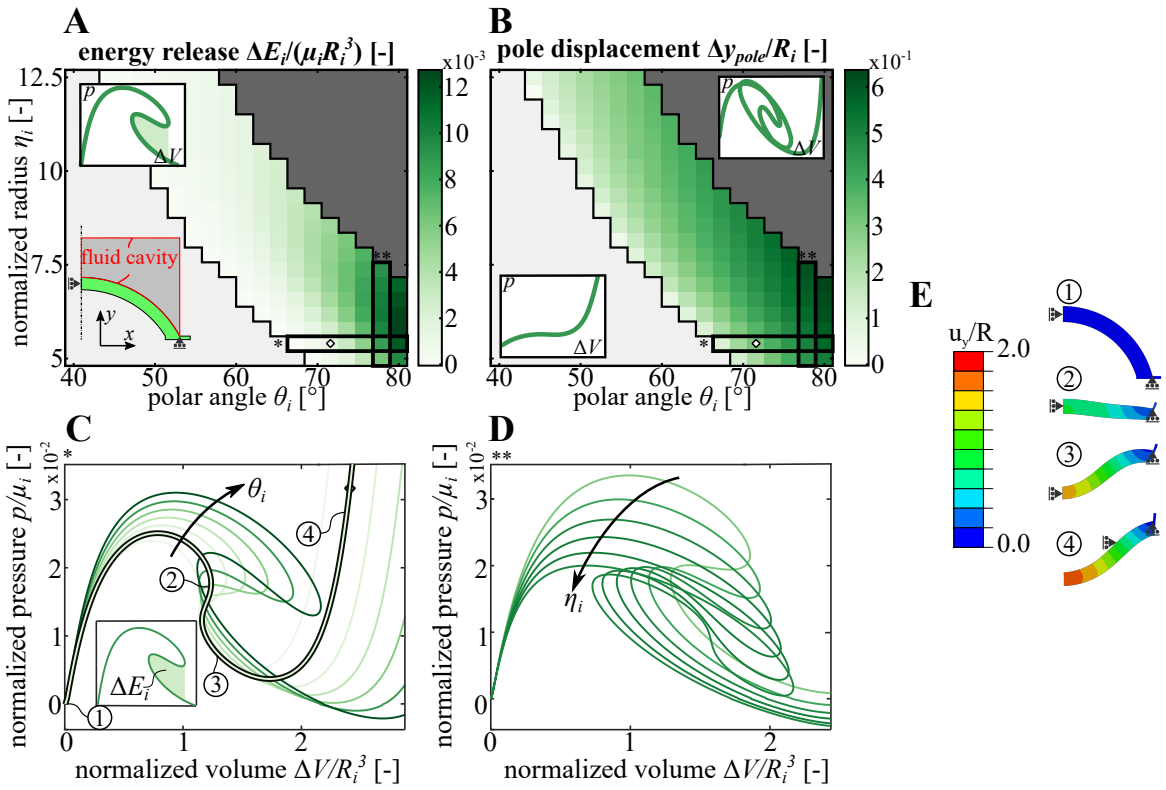

Fig. S15. Axisymmetric simulations of the inner cap. A-B. Evolution of the (**A**) normalized energy released and (**B**) pole displacement as a function of the normalized radius, η_i, and the polar angle, θ_i. **C-D.** Pressure-volume curves of the inner cap for (**D**) varying polar angle and (**E**) normalized radius. **E.** Numerical snapshots of an inner cap characterized by $\eta_i = 5.4$ and $\theta_i = 74^\circ$ at (1) rest, (2) before snapping, (3) after snapping, and (4) upon further inflation.

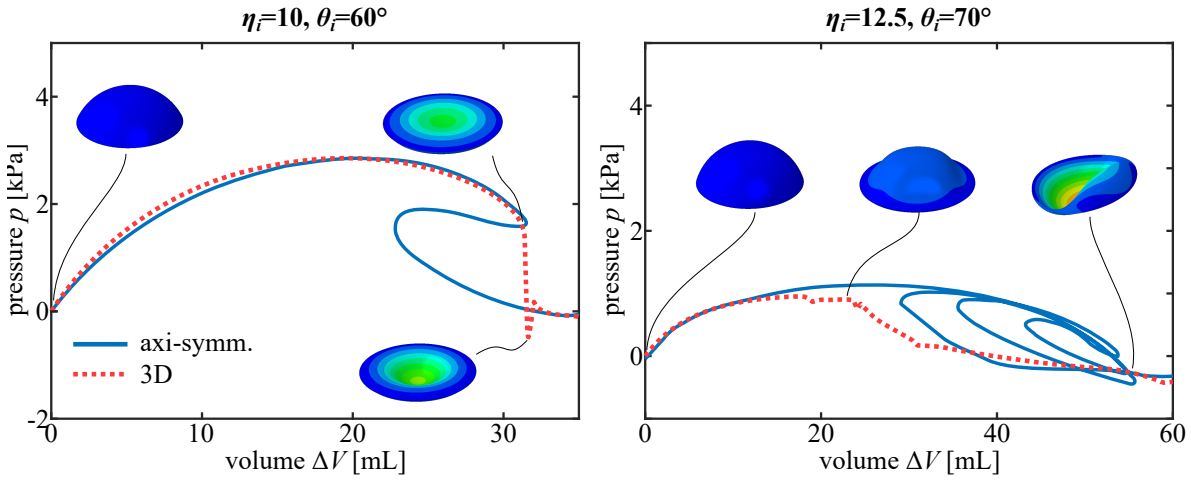

Fig. S16. Asymmetric deformation emerges in designs with self-crossing pressure-volume curves. Pressure-volume curve for an inner cap with $(\eta_i,\ \theta_i) = (10, 60°)$ (left) and $(12.5, 70°)$ (right) as predicted by our axisymmetric (back solid lines) and 3D (dashed blue lines) simulations. We find that caps for which the axisymmetric simulations predict a self crossing pressure-volume curve typically deform asymmetrically.

Finally, in Fig. S17 we present results for the outer cap. More specifically, in Fig. S17A we show the evolution of the stored energy at $p_o/\mu_o = 0.5$, E_0, as a function of the polar angle θ_o and the normalized radius η_o. The energy increases monotonically with increasing θ_o, almost irrespective of η_o.

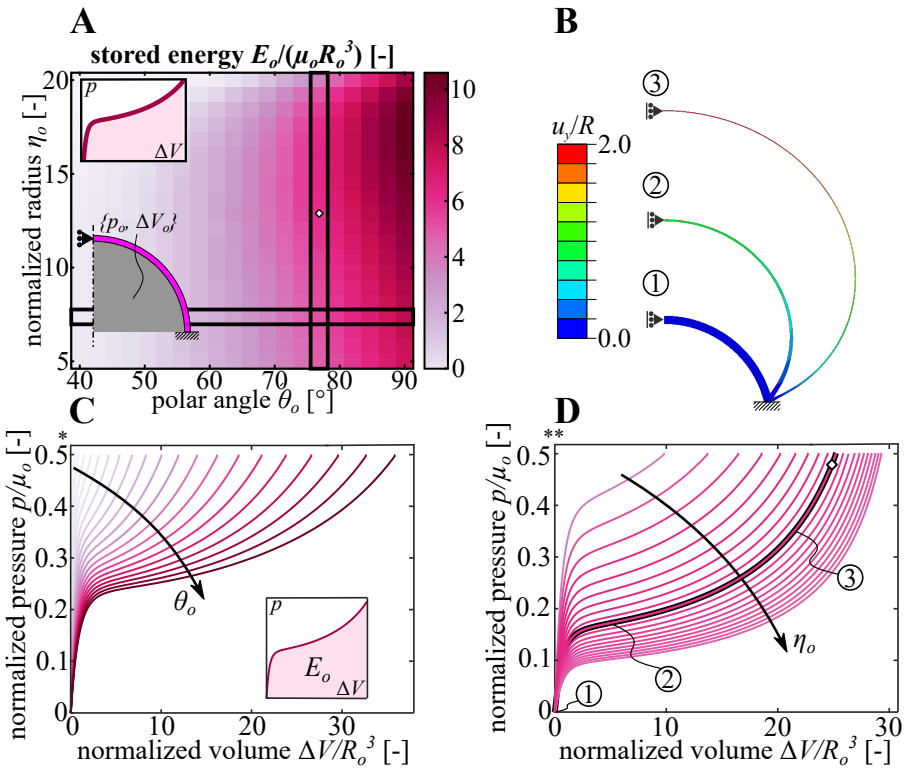

Fig. S17. Axisymmetric simulations of the outer cap. A. Evolution of the normalized stored energy at $p/\mu_o = 0.5$, $E_o/(\mu_o R_o^3)$, as a function of the normalized radius η_o and the polar angle θ_o. **B.** Numerical snapshots of an outer cap characterized by $\eta_i = 12.9$ and $\theta_i = 77°$ at different levels of inflation. **C-D.** Normalized pressure-volume curves for varying (**C**) θ_o and (**D**) η_o.

Section S5. Mass-spring model to predict the jump height

Our quasi-static FE simulations allow us to efficiently explore the design space and calculate ΔE and Δy_{pole} for a large number of designs. However, since they do not account for dynamic effects, they cannot be used to directly characterize the ability of the actuators to jump. To overcome this limitation, as described in the main text we establish a simple mass-spring model (see Fig. S18) that takes the FE results as input and predicts the jump height.

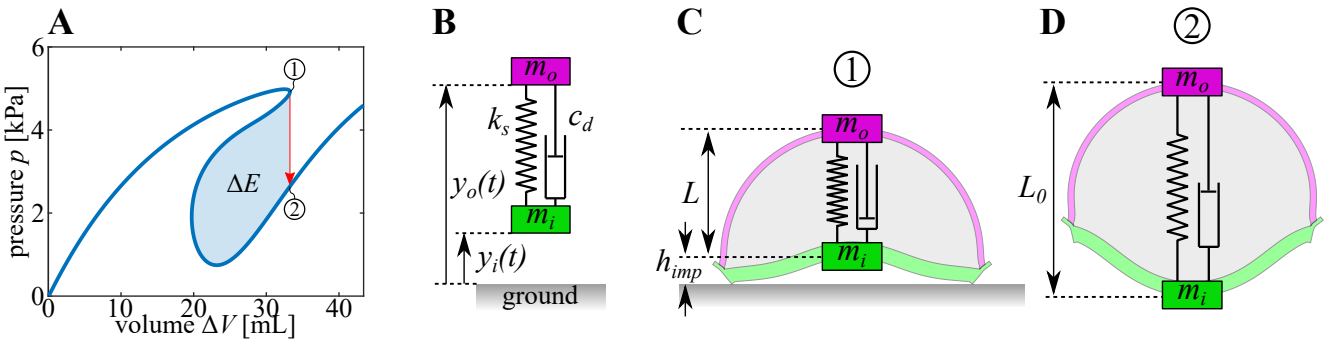

Fig. S18. Mass-spring model to predict jump height. A. Pressure-volume curve for Design C as predicted by our FE simulations. **B.** Our spring-mass model comprise two rigid masses, m_i and m_o, constrained to move vertically. We choose m_i and m_o to be equal to the mass of the inner and outer cap, respectively, and to be located at their corresponding poles. **C.** We assume that the mechanical system stores an amount of energy equal to ΔE in the numerically predicted configuration immediately before snapping. **D.** We assume that the mechanical system is stress-free in the numerically predicted configuration immediately after snapping.

Specifically, to solve for the jumping height of the actuator we determine the position of the individual masses, $y_i(t)$ and $y_o(t)$ as a function of time. The differential equations describing the motion of the model are

$$\begin{bmatrix} m_i & 0 \\ 0 & m_o \end{bmatrix} \begin{bmatrix} \ddot{y}_i \\ \ddot{y}_o \end{bmatrix} + \begin{bmatrix} c_d & -c_d \\ -c_d & c_d \end{bmatrix} \begin{bmatrix} \dot{y}_i \\ \dot{y}_o \end{bmatrix} + \begin{bmatrix} k_s & -k_s \\ -k_s & k_s \end{bmatrix} \begin{bmatrix} y_i \\ y_o \end{bmatrix} = \begin{bmatrix} -m_i g - k_s L_0 \\ -m_o g + k_s L_0 \end{bmatrix}, \quad [15]$$

where g is the gravitational acceleration ($g = 9.81$ m/s^2). To determine $y_i(t)$ and $y_o(t)$, we define $v_i = \dot{y}_i$ and $v_o = \dot{y}_o$ and transform Eqs. [15] into a first-order ODE system of the type

$$\dot{\mathbf{Y}} = \mathbf{A}\mathbf{Y} + \mathbf{B}, \quad [16]$$

where

$$\mathbf{Y} = \begin{bmatrix} y_i \\ y_o \\ v_i \\ v_o \end{bmatrix}, \quad \mathbf{A} = \begin{bmatrix} 0 & 0 & 1 & 0 \\ 0 & 0 & 0 & 1 \\ \frac{-k_s}{m_i} & \frac{k_s}{m_i} & \frac{-c_d}{m_i} & \frac{c_d}{m_i} \\ \frac{k_s}{m_o} & \frac{-k_s}{m_o} & \frac{c_d}{m_o} & \frac{-c_d}{m_o} \end{bmatrix}, \quad \mathbf{B} = \begin{bmatrix} 0 \\ 0 \\ -g - \frac{k_s L_0}{m_i} \\ -g + \frac{k_s L_0}{m_o} \end{bmatrix}. \quad [17]$$

We then write the solution for the homogeneous system $\dot{\mathbf{Y}} = \mathbf{A}\mathbf{Y}$ as

$$\mathbf{Y}_h = a\mathbf{P}_1 + b\left[\mathbf{P}_1 t + \mathbf{P}_2\right] + c\mathbf{P}_3 e^{\lambda_3 t} + d\mathbf{P}_4 e^{\lambda_4 t}, \quad [18]$$

where λ_i are the eigenvalues obtained by solving the characteristic equation $\det(\mathbf{A} - \lambda\mathbf{I}) = 0$

$$\begin{aligned} \lambda_1 &= \lambda_2 = 0, \\ \lambda_3 &= \frac{-c_d m_i - c_d m_o - \sqrt{m_i + m_o}\sqrt{c_d^2 m_i + c_d^2 m_o - 4k_s m_i m_o}}{2m_i m_o}, \\ \lambda_4 &= \frac{-c_d m_i - c_d m_o - \sqrt{m_i + m_o}\sqrt{c_d^2 m_i + c_d^2 m_o - 4k_s m_i m_o}}{2m_i m_o}, \end{aligned} \quad [19]$$

and $\mathbf{P}_i$ are the corresponding eigenvectors

$$\begin{aligned} \mathbf{P}_1 &= \begin{bmatrix} 1 & 1 & 0 & 0 \end{bmatrix}^T, \\ \mathbf{P}_2 &= \begin{bmatrix} 0 & 0 & 1 & 1 \end{bmatrix}^T, \\ \mathbf{P}_3 &= \begin{bmatrix} \frac{2m_o^2}{c_d m_i + c_d m_o + \sqrt{m_i + m_o}\sqrt{c_d^2 m_i + c_d^2 m_o - 4k_s m_i m_o}} & \frac{2m_i m_o}{c_d m_i + c_d m_o + \sqrt{m_i + m_o}\sqrt{c_d^2 m_i + c_d^2 m_o - 4k_s m_i m_o}} & -\frac{m_o}{m_i} & 1 \end{bmatrix}^T, \\ \mathbf{P}_4 &= \begin{bmatrix} \frac{2m_o^2}{c_d m_i + c_d m_o - \sqrt{m_i + m_o}\sqrt{c_d^2 m_i + c_d^2 m_o - 4k_s m_i m_o}} & \frac{2m_i m_o}{c_d m_i + c_d m_o - \sqrt{m_i + m_o}\sqrt{c_d^2 m_i + c_d^2 m_o - 4k_s m_i m_o}} & -\frac{m_o}{m_i} & 1 \end{bmatrix}^T. \end{aligned} \quad [20]$$

Moreover, a, b, c, d are constants of integration. Next, we determine the particular solution $\mathbf{Y}_p$ of the system of ODE through the method of variation of parameters as

$$\mathbf{Y}_p = \mathbf{\Phi}(t) \int \Phi^{-1}(t) B \mathrm{d}t, \tag{21}$$

where $\mathbf{\Phi}(t)$ is the fundamental matrix of the system

$$\mathbf{\Phi}(t) = \begin{bmatrix} \mathbf{P}_1 & \mathbf{P}_1 t + \mathbf{P}_2 & \mathbf{P}_3 e^{\lambda_3 t} & \mathbf{P}_4 e^{\lambda_4 t} \end{bmatrix}. \tag{22}$$

We then write the general solution of the system of ODE as

$$\mathbf{Y} = \mathbf{Y}_h + \mathbf{Y}_p \tag{23}$$

and determine the constants of integration by applying the initial condition

$$\mathbf{Y}^0 = \begin{bmatrix} y_i^0 & y_o^0 & v_i^0 & v_o^0 \end{bmatrix}^T = \begin{bmatrix} h_{imp} & h_{imp} + L & 0 & 0 \end{bmatrix}^T. \tag{24}$$

In all our analyses, we release the system at $t = 0$ and account for the collision between m_i and the ground by resetting the variables when a negative height $y_i(t)$ is calculated:

$$\text{if} \quad y_i(t_i) < 0 : \begin{cases} y_i(t_i) = 0 \\ v_i(t_i) = -\alpha \cdot v_i(t_{i-1}) \end{cases}, \tag{25}$$

where α is the coefficient of restitution. Note that $\alpha = 0$ is equivalent to a fully plastic collision and $\alpha = 1$ corresponds to a fully elastic collision with conservation of linear momentum. In all our analyses we use $\alpha = 0.5$, as we find that this gives good agreement between the predicted and experimentally measured jumping height.

In Fig. S19 we show the evolution of both y_i and y_o as predicted by the spring-mass model for Designs C and D. In the plots, we also compare the analytical solution to that obtained by integrating Eqs. (17) with the numerical solver `ODE45` of Matlab and, as expected, find perfect agreement between the two.

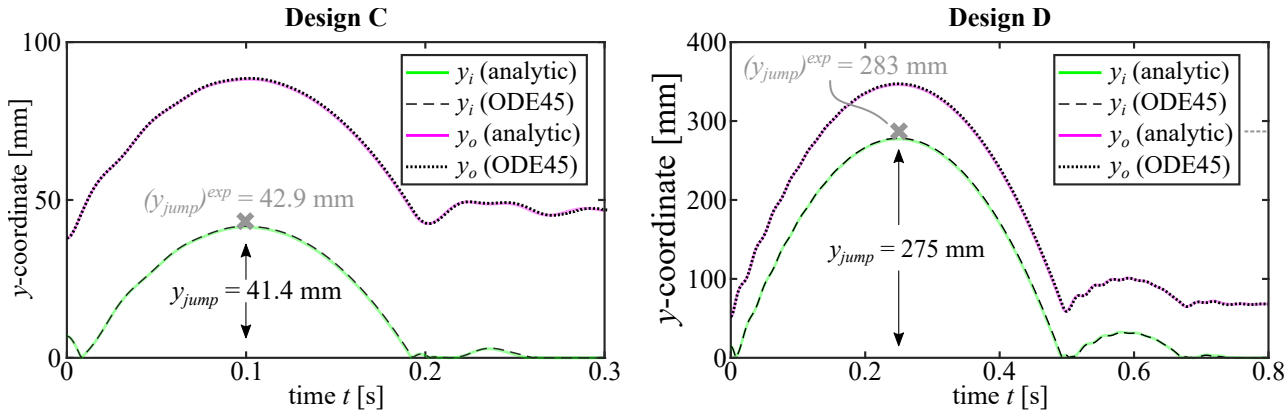

Fig. S19. Jump height prediction of the inflatable actuators. Evolution of both y_i and y_o as predicted by solving Eq. (17) analytically (continuous lines) and numerically via `ODE45` of Matlab (dashed lines) for Designs C and D.

Section S6. Additional results

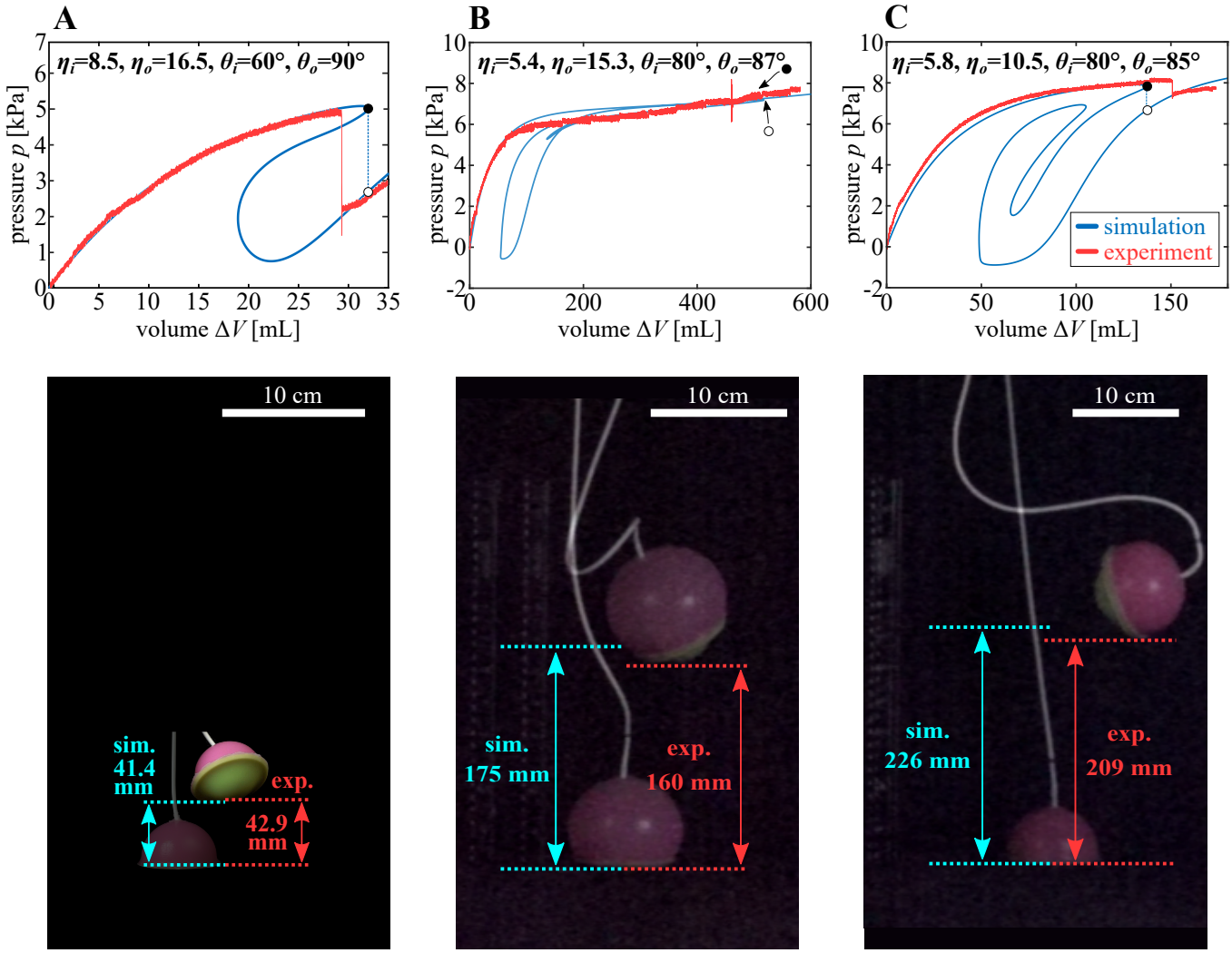

Fig. S20. Validation of the spring-mass model. To verify the validity of our simple mass-spring model, we focus on three designs with (**A**) (η_i, θ_i, η_o, θ_o, μ_i/μ_o)= $(8.5, 60^\circ, 16.5, 90^\circ, 5.8)$ (Design C), (**B**) $(5.4, 80^\circ, 15.3, 87^\circ, 5.8)$, and (**C**) $(5.8, 80^\circ, 10.5, 85^\circ, 5.8)$ and compare the experimentally measured jump heights ($h_{jump} = 42.9$ mm, 160 mm, and 209 mm, respectively) to the predicted ones ($h_{jump} = 41.4$ mm, 175 mm, and 226 mm, respectively). On the top, for each actuator we show the numerical (blue lines) and experimental (red lines) pressure-volume relations. On the bottom, we show experimental snapshots of the actuators before ischoric snap-through and at the highest point after jump. The good agreement between numerical and experimental results for all designs confirms the validity of our analyses.

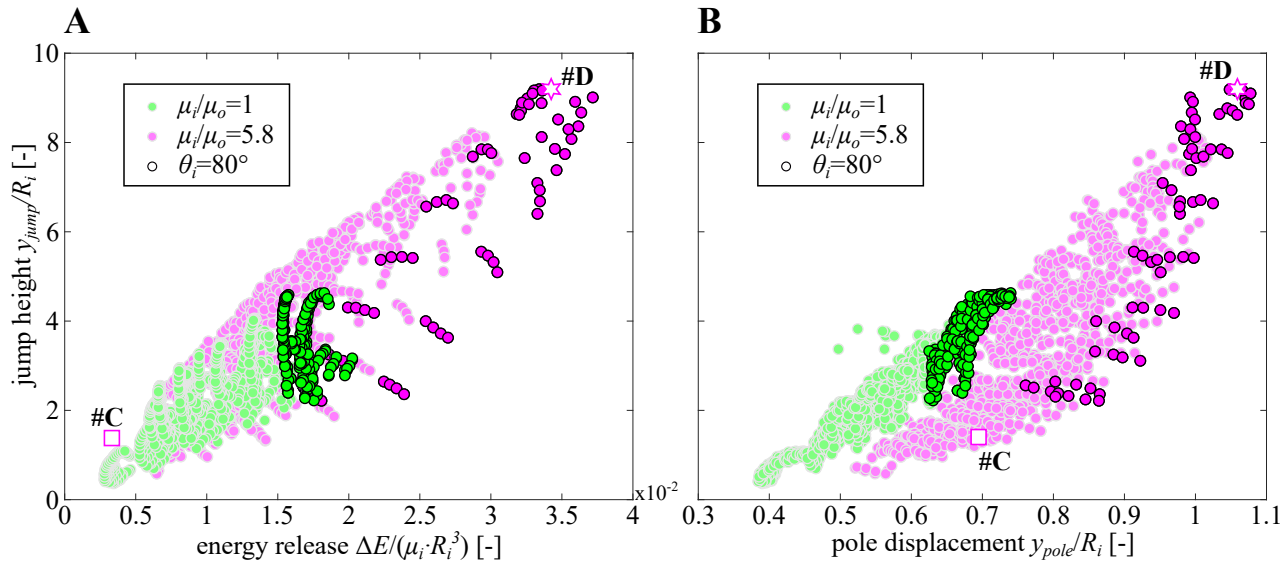

Fig. S21. Improving the performance our soft fluidic actuators through a grid search. Jump height vs. energy released (**A**) and jump height vs. pole displacement (**B**) as predicted by our analyses for 4800 actuators with $\theta_i \geq 70°$, $\eta_i \leq 8$, and $\theta_o \geq 76°$.

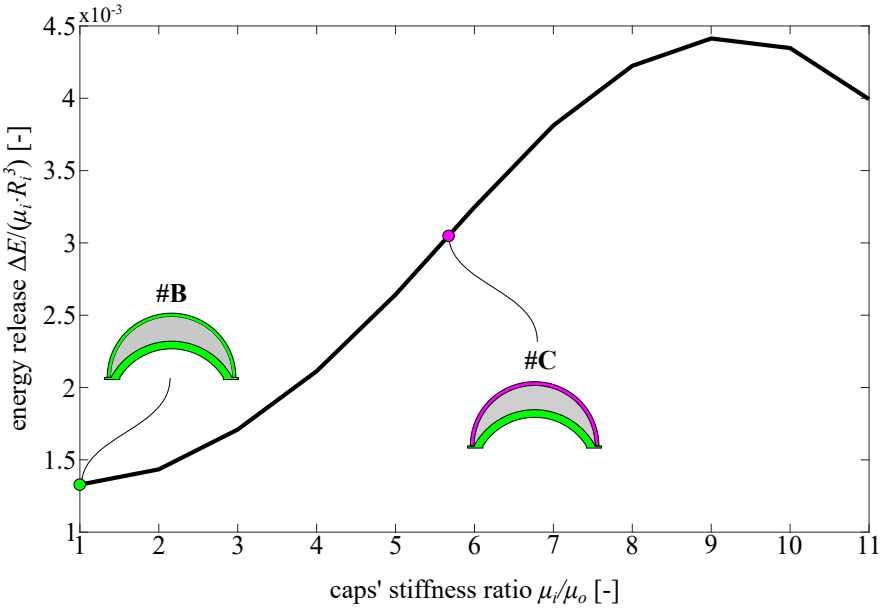

Fig. S22. Influence of the outer cap stiffness on the actuators' response. Energy release vs. ratio of the caps' stiffness for an actuator with $(\eta_i, \theta_i, \eta_o, \theta_o) = (8.5, 60°, 16.5, 90°)$. Note that for $\mu_i/\mu_o = 1$ and 5.8 the actuator corresponds to Designs B and C, respectively. We find that for this geometry, there exists a stiffness ratio $(\mu_i/\mu_o \sim 9)$ for which the energy released by the system during snapping is maximized.

Movie S1. Snapping of spherical caps results in a sudden release of elastic energy. When subjected to uniform external pressure, a spherical cap undergoes isochoric snap-through, i.e. a sudden loss of internal pressure at constant volume. This instability causes the sudden release of elastic energy as well as a fast displacement of the cap's pole.

Movie S2. Fast fluidic soft robots inspired by shell snapping. Our soft fluidic actuators comprise two spherical caps connected at their base. Upon inflation, the inner cap snaps at constant volume and the system suddenly releases elastic energy. To characterize the highly non-linear mechanical response of our actuators we use a combination of finite element simulations and experiments.

Movie S3. Isochoric snapping enables jumping in fluidic soft robots. Snapping can be exploited to make our actuators jump even when inflated at a slow rate. For this to happen, both the amount of energy released during isochoric snapping and the magnitude of the pole displacement during the transition have to be large enough.

Movie S4. Simplified mass-spring model to predict jump height. To characterize the ability of our actuators to jump, we use a simplified mass-spring model that takes the FE results as inputs and predicts the jump height.

Movie S5. Improving jumper design to increase jump height. By exploring the design space and simulating the jumper through finite element analysis and a simplified mass-spring model, we identify a design with a 5-fold increase in jump height compared to Design C.

Movie S6. Inflatable actuator with repetitive jumping. Most of our actuators can be simply reset and brought back to the initial configuration through vacuum and, therefore, can take off repetitively. ,